A Stochastic Parameterization of Non-Orographic Gravity Waves Induced Mixing for Mars Planetary Climate Model

Jiandong Liu, Ehouarn Millour, François Forget, François Lott, Jean-Yves Chaufray

JGR Planets

RESEARCH ARTICLE
10.1029/2025JE009188

A Stochastic Parameterization of Non-Orographic Gravity Waves Induced Mixing for Mars Planetary Climate Model

Jiandong Liu[1,2], Ehouarn Millour[1], François Forget[1], François Lott[1], and Jean-Yves Chaufray[3]

[1]LMD/IPSL, Sorbonne Université, ENS, Université PSL, École Polytechnique, Institut Polytechnique de Paris, CNRS, Paris, France, [2]Laboratoire de Physique et Chimie de l'Environnement et de l'Espace, CNRS/Université d'Orléans, UMR 7328, Orléans, France, [3]LATMOS, CNRS, Sorbonne Université, Université Versailles St-Quentin, Paris, France

Key Points:

- Turbulence from non-orographic gravity waves is parameterized in the Mars Planetary Climate Model
- Simulations are compatible with observations
- Mars has an irregular turbopause depending on the season and local solar time

Correspondence to:
J. Liu,
jiandong.liu@lmd.ipsl.fr

Citation:
Liu, J., Millour, E., Forget, F., Lott, F., & Chaufray, J.-Y. (2025). A stochastic parameterization of non-orographic gravity waves induced mixing for Mars Planetary Climate Model. *Journal of Geophysical Research: Planets*, *130*, e2025JE009188. https://doi.org/10.1029/2025JE009188

Received 16 MAY 2025
Accepted 2 SEP 2025

Author Contributions:
Conceptualization: Jiandong Liu, François Lott
Formal analysis: Jiandong Liu
Investigation: Jiandong Liu, Jean-Yves Chaufray
Methodology: Jiandong Liu, François Lott, Jean-Yves Chaufray
Resources: Ehouarn Millour, François Forget
Software: Jiandong Liu, Ehouarn Millour, François Forget
Supervision: Ehouarn Millour, François Forget, François Lott
Validation: Jiandong Liu, Ehouarn Millour, François Forget
Visualization: Jiandong Liu
Writing – original draft: Jiandong Liu
Writing – review & editing: Jiandong Liu

Abstract This paper presents a formalism of mixing induced by non-orographic gravity waves (GWs) to integrate with the stochastic GWs scheme in the Mars Planetary Climate Model. We derive the formalism of GWs and their mixing under the same assumptions, integrating the two schemes within a unified framework. Specifically, a surface-to-exosphere parameterization of GW-induced turbulence has been derived in terms of the eddy diffusion coefficient. Simulations show that the coefficient is on the order of 10^4 to 10^9 cm^2 s^{-1} and a turbopause is at altitudes of 70–140 km, varying with seasons. The triggered mixing has minor effects on model temperatures, yet it substantially impacts upper atmospheric abundances. Simulations are consistent with observations from the Mars Climate Sounder and the Neutral Gas and Ion Mass Spectrometer. Mixing enhances the tracer transports in the middle and upper atmosphere, governing the dynamics of these regions. The scheme reveals how non-orographic GW-induced turbulence can regulate upper atmospheric processes, such as tracer escape.

Plain Language Summary Non-orographic gravity waves are caused by atmospheric motions like convection and jet streams. As these waves rise, they grow and eventually break due to thinning air. This releases energy and creates swirling motions called turbulent eddies at various scales, a phenomenon known as turbulence. These chaotic swirling motions mix the gases quickly, known as eddy diffusion or mixing. This process is much faster than molecular diffusion, the slow, random spread of molecules from regions of high to low concentration. This study presents a new way to model eddy diffusion driven by non-orographic gravity waves in Mars' atmosphere. The method works with existing climate models and uses consistent physics to link wave activity with turbulent mixing. The strength of mixing, described by the eddy diffusion coefficient, ranges from 10^4 to 10^9 cm^2 s^{-1}. The turbopause, the altitude where eddy diffusion and molecular diffusion are equally strong, lies between 70 and 140 km, depending on local time and season. While this mixing has little effect on temperature, it significantly alters how gases are distributed in the upper atmosphere. The model results match spacecraft observations and show that wave-driven turbulence plays a key role in transporting gases and supporting atmospheric escape on Mars.

1. Introduction

Martian upper atmospheric dynamics govern the transport and escape of the planet's atmosphere (Benna et al., 2019; M. S. Chaffin et al., 2021; Fedorova et al., 2020; Jakosky et al., 2017; Stone et al., 2020; Yiğit et al., 2021), playing a vital role in understanding the evolution of Mars' habitability (M. Chaffin et al., 2017; Jakosky et al., 2017; Yiğit, 2021). Abundances of Martian upper atmospheric neutrals, sampled by the Neutral Gas and Ion Mass Spectrometer (NGIMS) (Benna & Lyness, 2014; England et al., 2017; Mahaffy, Benna, King, et al., 2015) and other instruments (Creasey et al., 2006; Nakagawa et al., 2020; Vals et al., 2019), have revealed unexpected density fluctuations (Fritts et al., 2006; Li et al., 2021; J. Liu et al., 2019; Mahaffy, Benna, Elrod, et al., 2015; Stone et al., 2018) that cannot be explained by model simulations, even when internal and external forcings are well prescribed (Forget et al., 1999; González-Galindo et al., 2009; J. Liu et al., 2023).

Generally, orographic gravity waves (GWs) have limited effects on layers above the middle atmosphere (Forget et al., 1999; Lott & Miller, 1997). Consequently, investigations have focused primarily on forcings from the lower atmosphere and, unsurprisingly, on non-orographic GWs (J. Liu et al., 2023; Roeten et al., 2022; Yiğit et al., 2015). The turbulence generated by non-orographic GWs has been proposed as the cause of the observed

density fluctuations (Beasley & Hodges, 1973; Creasey et al., 2006; Fritts et al., 2006; M. B. McElroy & Donahue, 1972; M. McElroy et al., 1976; Rodrigo et al., 1990; Yoshida et al., 2022).

However, a surface-to-exosphere gravity wave-mixing scheme was not available for a General Circulation Model (GCM), such as the Mars Planetary Climate Model (Mars PCM), for several reasons: (a) There is a lack of full-layer non-orographic gravity wave schemes capable of producing simulations that match observations both below and above the middle atmosphere (J. Liu et al., 2023; Roeten et al., 2022). Consequently, it is impossible to develop a GW-mixing scheme that is consistent with the gravity wave scheme, as a large portion of the waves become saturated in the thermosphere (Beasley & Hodges, 1973; Vals et al., 2019; Yiğit, 2021; Yiğit et al., 2021). (b) The mechanism of GWs-induced turbulence is not fully understood (H.-L. Liu, 2021).

The gravity wave Eddy Diffusion Coefficient (EDC) was proposed as a concept analogous to molecular diffusivity to describe the turbulence induced by gravity waves (Barnes et al., 1996; Beasley & Hodges, 1973; Hodges, 1967, 1969; Hines, 1974; Holton, 1982; Holton & Schoeberl, 1988; R. S. Lindzen, 1981; Leovy, 1982; M. B. McElroy & Donahue, 1972; Strobel, 1989; Shimazaki, 1989; Slipski et al., 2018; Yoshida et al., 2022). These turbulence and mixing are proposed to be induced by superadiabatic temperature gradients at or above altitudes where the gravity waves are saturated (Hodges, 1967, 1969; Holton, 1982; Hines, 1974; R. S. Lindzen, 1981). Inspired by this idea, a polynomial relationship between the eddy diffusivity and the vertical wavelength of waves was developed (Hines, 1974; Hodges, 1969), in which the maximum diffusivity is on the order of 10^6 to 10^8 cm^2 s^{-1} for waves with horizontal wavelengths ranging from 10 to 1,000 km. Additionally, an EDC of 10^6 to 10^8 cm^2 s^{-1} has been estimated for the Mars upper atmosphere using this type of relationship (Barnes et al., 1996; Beasley & Hodges, 1973; Strobel, 1989). All those early attempts are beneficial for 1-D (vertical) monochromatic wave analysis. However, these formalisms may lack consideration of wave saturation and, therefore, are not suitable for a model that includes the upper atmosphere.

R. S. Lindzen (1981) developed a set of equations to describe turbulence caused by wave saturation, assuming that the vertical temperature gradient induced by saturated waves should never surpass the environmental lapse rate. Holton (1982) and Weinstock (1982) derived a relationship between the pseudo momentum (Eliassen-Palm flux, EP-flux) and the eddy diffusion coefficient, based on the formalism and assumptions of R. S. Lindzen (1981). Many of the implementations of R. S. Lindzen (1981) and Holton (1982) have been tested in 3-D GCMs below the thermosphere (Garcia & Solomon, 1985; Holton & Schoeberl, 1988; R. Lindzen & Forbes, 1983; Théodore et al., 1993) or in 2-D GCMs that include the thermosphere (Imamura et al., 2016). Simulations show that the eddy diffusivity influences the vertical transport of chemical tracers in the mesosphere and higher layers (Holton & Schoeberl, 1988; Imamura et al., 2016). The limitations of R. S. Lindzen (1981) and Holton (1982) are (a) the saturation conditions are applied too broadly (R. Lindzen & Forbes, 1983; Imamura et al., 2016), and (b) the derivations are conducted below the lower thermosphere.

EDC values ranging from 1×10^4 to 10^8 cm^2 s^{-1} have been derived from observations of multiple Martian missions (Anderson & Leovy, 1978; M. B. McElroy & Donahue, 1972; Nier & McElroy, 1976; Rosenqvist & Chassefière, 1995; Shimazaki, 1989; Slipski et al., 2018; Yoshida et al., 2022). These retrievals leverage the life cycle of specific, long-lived atmospheric species (such as CO) (Rodrigo et al., 1990; Yoshida et al., 2022), during which fluctuations in the species' abundances must be driven by eddy diffusion (Rodrigo et al., 1990; Shimazaki, 1989). Intensive Ar transport, caused by mixing-circulation interaction, has been observed in the Mars lower atmosphere polar region (Forget, 2004; Sprague et al., 2004), suggesting an EDC of 10^8 cm^2 s^{-1} during clear-sky seasons and 10^9 cm^2 s^{-1} during dusty seasons. A power law relationship between eddy diffusivity and the species densities has been found to be realistic for the middle atmosphere (Leovy, 1982; Von Zahn et al., 1980; Yoshida et al., 2022), implying an EDC of 10^6 to 10^7 cm^2 s^{-1} at altitudes of 70–105 km. EDCs estimated from Viking observations are on the order of 10^7 to 10^9 cm^2 s^{-1} at altitudes of 110–170 km (M. B. McElroy & Donahue, 1972; M. McElroy et al., 1976; Nier & McElroy, 1976). Rodrigo et al. (1990) estimated an EDC ranging from 10^7 to 10^8 cm^2 s^{-1} for the upper atmosphere below 160 km, with a turbopause at 140 km. Shimazaki (1989) suggested that an EDC of 5×10^7 cm^2 s^{-1} is needed to reproduce atomic oxygen observations in the upper atmosphere made by Mariner 6 and 7. The Homopause, inferred from NGIMS-observed $N_2/^{40}Ar$ ratio (Mahaffy, Benna, Elrod, et al., 2015), shows substantial variations from 75 to 140 km, depending on the season (Jakosky et al., 2017). Further investigation suggests a co-evolution of the turbopause with the homopause (Slipski et al., 2018). All these retrieved turbulence coefficients provide quantitative constraints for a realistic GW turbulence scheme.

The mixing scheme described in this paper builds on the foundation of the surface-to-exosphere gravity wave scheme developed by J. Liu et al. (2023), which is an improvement and vertical extension of Lott et al. (2012). We revisit the seminal formalism proposed by R. S. Lindzen (1981), Holton (1982), and Weinstock (1982), in which turbulence is assumed to be generated by wave saturation. This idea has now been refined as "turbulence arises from the divergence of wave momentum." This new concept is then applied to the entire atmosphere using wave-ensembles theory designed by Lott et al. (2012) and Lott and Guez (2013). In Section 2, we review the derivation of the non-orographic GWs formalism using the extended Non-Superadiabatic Principle (NSP). The goal is to provide a theoretical interface for the induced mixing formalism. In Section 3, a mixing scheme is designed by using the extended NSP and the theoretical interface. A comprehensive formula for the eddy diffusion coefficient is derived from both theoretical and empirical analyses. Section 4 presents numeric simulations using the Mars Planetary Climate Model. The simulated results are compared with observations from both MCS and NGIMS. Summaries and future perspectives are outlined in Section 5.

2. Non-Orographic Gravity Waves

The original design of the non-orographic gravity wave scheme described in this paper was developed by Lott et al. (2012), in which the waves are represented using stochastic wave ensembles (Lott & Guez, 2013). This elegant design accumulates wave momentum over a few model time steps and then employs a first-order Auto-Regressive algorithm (AR-1) to transfer the momentum to the mean zonal flow. The scheme performs well for the LMDZ.EARTH model, which excludes the upper atmosphere (De la Cámara et al., 2014), successfully reproducing the well-known Quasi-Biennial Oscillation (QBO) in the Earth's mesosphere (Lott & Guez, 2013). The design was adapted and refined by J. Liu et al. (2023) to operate within the Mars Planetary Climate Model (Mars PCM), a surface-to-exosphere GCM (González-Galindo et al., 2009). The adapted scheme reproduces temperature structures below 100 km consistent with MCS observations and simulates upper atmospheric abundances compatible with NGIMS measurements (J. Liu et al., 2023).

We consider that at each model (physical) step t (of duration δt), the wave-induced vertical velocity w' is represented as a weighted sum of M monochromatic waves' amplitudes $\hat{w}_j$: $w' = \sum_{j=1}^{M} C_j \hat{w}_j$, where the weights satisfy $\sum_{j=1}^{M} C_j^2 = 1$. Following (Lott et al., 2012), we use $M = 8$ waves. To evaluate the wave amplitude $\hat{w}_j$, we randomly assign the horizontal wavenumber k_j and l_j, phase speed c_j, orientation $\vartheta \in [0, 2\pi]$, and initial momentum flux at a specific reference (launch) altitude z_r. The vertical propagation of $\hat{w}_j$ from one model level z_{ll} to the next z_{ll+1} is then treated by a Wentzell-Kramers-Brillouin (WKB) approximation.

In this section, we will present the detailed formalism of J. Liu et al. (2023) to provide a common framework for both non-orographic GWs and wave-induced turbulence.

2.1. Eliassen-Palm Flux

Rather than treating the waves directly, their effects are accounted for through their pseudo momentum, specifically the Eliassen-Palm (EP) flux (Fritts, 1984; Lott et al., 2012; Lott & Guez, 2013; Yiğit et al., 2008). When rotation is neglected, the EP-flux is assumed to be a constant at its launch altitude (Fritts & Alexander, 2003). For jth monochromatic wave at the launching (reference) level z_r, where the waves are generated, the EP-flux is given by,

$$\vec{\mathrm{E}}_j^{z_r}(k_j, l_j, \omega_j) = \Re\left\{\rho_r \frac{\hat{u}\hat{w}^*}{2}\right\} \tag{1}$$

where ρ_r is the atmospheric mass density at the launching (reference) altitude; $\hat{u}$ and $\hat{w}$ are zonal and vertical wind amplitudes; $\Re$ denotes the real part; k_j, l_j horizontal wavenumbers, and $\vec{k} = (k_j, l_j)$; $\omega_j = \vec{k}_j c_j$ is the absolute frequency of the wave, with c_j representing the phase speed. In the Mars PCM, the maximum truncation of $\vec{E}_j^{z_r}$ equals 5×10^{-4} kg m^{-1} s^{-2} (J. Liu et al., 2023).

The zonal wind amplitude $\hat{u}$ depends on the vertical wind amplitude $\hat{w}$ through waves' vertical wave number m, as described by the "polarized material equation" (Fritts, 1984; Fritts & Alexander, 2003),

$$\hat{u} = -\frac{m}{|\vec{k}|}\hat{w}\frac{\vec{k}}{|\vec{k}|} \tag{2}$$

The EP-flux can be rewritten as a function excluding $\hat{u}$ by inserting (Equation 2 into Equation 1), which reads,

$$\vec{E}_j^{z_r}(k_j, l_j, \omega_j) = \Re\left\{\rho_r \frac{\hat{u}\hat{w}^*}{2}\right\} = -\rho_r \frac{\vec{k}}{2|\vec{k}|^2} m_j(z_r)|\hat{w}_j(z_r)|^2 \tag{3}$$

Equation 3 provides an expression for the EP-flux that includes solely the wave amplitude $\hat{w}_j$ (For convenience, the index j is dropped from m, k, l, and c). This implies that the EP-flux of a specific wave j depends solely on $\hat{w}_j$. Consequently, we will search for $\hat{w}_j$ from an appropriate wave equation within a hydrostatic atmosphere in the following sections.

2.2. Taylor-Goldstein Equation

The Taylor-Goldstein Equation (TGE) describes the evolution of the amplitude of small perturbations (i.e., $\hat{w}_j$ in this paper) in stably stratified, incompressible shear flows (Fritts, 1984; R. S. Lindzen, 1981). It has been widely used as the governing equation of the gravity wave theory (Lott et al., 2012; Yiğit et al., 2008), with its derivation detailed in references such as Nappo (2013).

The key to evaluating the life cycle of a specific monochromatic wave lies in tracking the behavior of $\hat{w}_j$, which is governed by the wave's pseudo momentum as expressed in Equation 3. Assuming a gravity wave with absolute (intrinsic) frequency $\omega_j \gg f$ (the Coriolis frequency), the vertical velocity (perturbation) w_j' of the jth harmonic satisfies,

$$w_j' = \Re\left\{\hat{w}_j(z)e^{z/2H}e^{i(k_j x + l_j y - \omega_j t)}\right\} \tag{4}$$

in which case the amplitude $\hat{w}_j$ satisfies the following Taylor-Goldstein Equation (TGE),

$$\frac{\partial^2 \hat{w}(z)}{\partial z^2} + \underbrace{\left(\frac{|\vec{k}|^2 N^2}{\Omega^2} + \frac{\vec{k}\left(\vec{u}_{zz} + \vec{u}_z/H\right)}{\Omega} - \frac{1}{4H^2}\right)}_{Q(z)}\hat{w}(z) = 0 \tag{5}$$

where $N^2 = g/T\Gamma$ represents the square of Brunt-Väisälä frequency; $\Gamma = \partial T/\partial z + g/c_p$ is the environmental lapse rate; g is the gravity acceleration, T the temperature, and $c_p(T)$ the specific heat capacity. The vertical coordinate z is the pseudo-altitude, defined as $z = H\ln(P_r/P)$, where P is the pressure, P_r the pressure at the wave reference altitude, and H the atmospheric scale height. $\vec{u}_{zz}$ is $\partial^2\vec{u}/\partial z^2$ and $\vec{u}_z$ is $\partial\vec{u}/\partial z$; $\Omega = \vec{k}\left(\vec{k}c/|\vec{k}| - \vec{\bar{u}}\right)$ is the wave's intrinsic frequency with Doppler shift; $\bar{u}$ the background winds.

In most circumstances, the last two terms of $Q(z)$ in Equation 5 are negligible, that is, $Q(z) \approx |\vec{k}|^2 N^2/\Omega^2$. Therefore, Equation 5 simplifies to,

$$\frac{\partial^2 \hat{w}(z)}{\partial z^2} + m_r^2 \hat{w}(z) = 0 \tag{6}$$

We define this approximated $Q(z)$ as the square of the (real) vertical wavenumber,

$$m_r^2 = \frac{|\vec{k}|^2 N^2}{\Omega^2} \tag{7}$$

We label the vertical wave number as m_r instead of m, where $m_r = \Re\{m\}$. This distinction is made to differentiate from $m_i = \Im\{m\}$, the imaginary part of m, which is induced by the turbulence of the wave. The m_i will be detailed in Section 2.4.2. Note that m_r changes slowly with altitude z.

All subsequent analysis is based on the wave Equation 6. Once the solution $\hat{w}$ of this wave equation is obtained, the wave's momentum flux is calculated using Equation 3. The form of $\hat{w}$ depends critically on the sign of the square of the Brunt-Väisälä frequency, N^2, as seen in Equations 6 and 7; note that $|\vec{k}|^2$ and Ω^2 are both positive.

2.3. Wentzell-Kramers-Brillouin Approximation

If m_r^2 were constant, (Equation 6) would be trivial to solve. However, since m_r^2 varies slowly with z, the Wentzell-Kramers-Brillouin (WKB) approximation applies (Holton, 1982; R. S. Lindzen, 1981),

$$\hat{w}(z) \approx A(z)|m_r|^{-1/2} \exp\left(i\int_0^z m d\zeta\right) \tag{8}$$

where $A(z)$ is an altitude-dependent constant for $\zeta \in$ [surface, top]; again, we define $m = m_r + im_i$ (with $i^2 = -1$) but neglect $\Im(m)$ (its physics and derivation follow in Sections 2.4.2). The real component $\Re(m)$ is obtained from (Equation 7) as,

$$m_r = -\frac{N|\vec{k}|}{\Omega}. \tag{9}$$

Note that $N < 0$, if $z > z_r$; thus $m_r > 0$ in (Equation 9) for $z > z_r$. The real part of the vertical wavenumber is sometimes represented as $m_r = N/(\bar{u} - c)$ for convenience since $\Omega = \vec{k}(\vec{k}c/|\vec{k}| - \vec{\bar{u}})$.

The WKB approximation can also be expressed recursively in altitude to eliminate the constant $A(z)$. Applying (Equation 8) to adjacent layers z_{ll} and z_{ll+1} and taking their ratios yields,

$$\hat{w}_j(z_{ll+1}) = \hat{w}_j(z_{ll})\sqrt{\frac{m_r(z_{ll})}{m_r(z_{ll+1})}}\exp\left(i\int_{z_{ll}}^{z_{ll+1}} m^{ave} d\zeta\right) \tag{10}$$

where $m^{ave} = (m(z_{ll}) + m(z_{ll+1}))/2$ and $A(z_{ll}) \approx A(z_{ll+1})$. Both Equations 8 and 10 represent Wentzel-Kramers-Brillouin (WKB) approximations of (Equation 6) for slowly varying m_r^2. Notably, (Equation 10) omits $A(z)$, enhancing its practical utility.

We now have nearly exact solutions for $\hat{w}_j$ through Equations 8 and 10, but two obstacles prevent their application to the EP-flux (Equation 3): (a) the need to determine m_i in WKB approximations, and (b) the real atmosphere effects (critical layer, saturation, and kinematical viscosity) modify the vertical evolution of $\hat{w}_j$. Both challenges are addressed by incorporating thermodynamic constraints during wave saturation (R. S. Lindzen, 1981) and accounting for kinematic viscosity (Lott et al., 2012).

2.4. Saturation, Critical Layer and Atmosphere Viscosity

Three factors govern the vertical evolution of $\hat{w}_j$: (a) wave saturation (and induced turbulence damping), where EP-flux peaks and releases (most of) momentum to the mean zonal flow as atmospheric density decreases exponentially (R. S. Lindzen, 1981; Lott et al., 2012); (b) critical layers that nullify wave momentum at Ω phase transitions (Lott et al., 2012; Lott & Guez, 2013); and (c) kinematic viscosity, particularly dominant in the upper atmosphere, which damps wave amplitude (Yiğit et al., 2008; J. Liu et al., 2023). These mechanisms are well-documented observationally Yiğit et al. (2015), Vals et al. (2019), J. Liu et al. (2019).

2.4.1. Wave Thermodynamics

As pointed out by Hodges (1967) and Hodges (1969), turbulence arises from localized superadiabatic regions (convective instabilities) triggered by gravity waves. R. S. Lindzen (1981) noted that wave saturation and the resulting turbulence limit vertical temperature gradients to the adiabatic lapse rate Γ. This implies that turbulence

suppresses the growth of superadiabatic regions (Hodges, 1969), maintaining vertical temperature gradients near the adiabatic lapse rate Γ (Fritts, 1984). This also suggests that a form of thermodynamic equilibrium is established during wave momentum release in the affected region.

For a monochromatic harmonic with vertical velocity w_j' given by Equation 4, the associated temperature amplitude $\delta\hat{T}$ resulting from the wave's work on the atmosphere can be derived from the thermodynamic energy equation in its polarized form,

$$i\vec{k}_j(c-\bar{u})\delta\hat{T} = \hat{w}_j e^{z/2H}\Gamma, \quad z \in [surface, top] \tag{11}$$

where $\Gamma = dT/dz + g/c_p$ is the environmental lapse rate. Notice $\Omega = \vec{k}(c-\bar{u})$, we can write it as $i\Omega\delta\hat{T} = \hat{w}_j e^{z/2H}\Gamma$. Note that the index j for phase speed and wavenumbers has been omitted for convenience.

From the thermodynamic energy Equation 11, one obtains,

$$\delta\hat{T} = \frac{\Gamma\hat{w}_j e^{z/2H}}{i\Omega} \tag{12}$$

Furthermore, we replace the vertical velocity amplitude $\hat{w}_j$ in (Equation 12) with its WKB approximation from (Equation 8), using $m_r = -N|\vec{k}|/\Omega$. Equation 12 then becomes,

$$\delta\hat{T} = \frac{-i\Gamma A|m_r|^{-1/2}e^{i\int_0^z m d\zeta}e^{z/2H}}{\Omega} \tag{13}$$

The $\delta\hat{T}$ in (Equation 13) depends on the stochastic parameters of a monochromatic wave and the background atmosphere, including the vertical wavenumber m, horizontal wavenumber $\vec{k}$, wave intrinsic frequency with Doppler shift Ω, environmental lapse rate Γ, and atmospheric density $\rho \propto e^{z/2H}$. The vertical evolution of $\delta\hat{T}$ is primarily governed by m_r, $\exp\int_0^z m d\zeta$, and $\exp z/2H$, while other terms are constants.

Let $L = -i\Gamma A|m_r|^{-1/2}e^{i\int_0^z m d\zeta}e^{z/2H}$, and thus $\delta\hat{T} = L/\Omega$. By differentiating Equation 13 with respect to z, the vertical temperature gradient induced by the wave's vertical velocity follows,

$$\frac{d\delta\hat{T}}{dz} = \frac{L}{\Omega^2}\left[\Omega\left(im + \frac{1}{2H}\right) - \frac{\partial\Omega}{\partial z}\right] \tag{14}$$

Considering $m = m_r + im_i$ and the vertical wavenumber m_r in (Equation 9), the real value of the temperature gradient (Equation 14) reads,

$$\begin{aligned}\Re\left\{\frac{d\delta\hat{T}}{dz}\right\} &= \frac{\Gamma A|m_r|^{-1/2}e^{-\int_0^z m_i d\zeta}e^{z/2H}m_r}{\Omega} \\ &= -\frac{\Gamma A|m_r|^{3/2}e^{-\int_0^z m_i d\zeta}e^{z/2H}}{N|\vec{k}|} \\ &= -\frac{\Gamma A|m_r|^{3/2}e^{\int_0^z(\frac{1}{2H}-m_i)d\zeta}}{N|\vec{k}|}, \quad z\in[surface, top]\end{aligned} \tag{15}$$

$A\Gamma/N|\vec{k}|$ varies slowly for a given harmonic. The terms $e^{z/2H}$, $|m_r|^{3/2}$, and $\exp\int_0^z m_i d\zeta$ dominate the growth of $\left|\Re\left(\frac{d\delta\hat{T}}{dz}\right)\right|$ as shown in (Equation 15). $|m_r|^{3/2}$ and $\exp -\int_0^z m_i d\zeta$ are induced by the wave-mean flow interaction. However, Equation 15 cannot be evaluated directly due to the unknown parameters m_i and A, requiring additional constraints for the solution.

2.4.2. Non-Superadiabatic Principle and $m_{i,s}$

Hodges (1967, 1969) were the first to explain that turbulence observed in the upper atmosphere can result from localized superadiabatic regions $\left(\left|\Re\left(\frac{d\delta\hat{T}}{dz}\right)\right| > \Gamma\right)$ induced by wave saturation. This turbulence, once triggered, suppresses further growth of these regions. This concept was implemented in practice by R. S. Lindzen (1981) and Holton (1982), assuming that the superadiabatic region within the thin layers around the wave saturation altitude is suppressed completely by the induced turbulence. We refer to this assumption as the Non-Superadiabatic Principle (NSP).

While the NSP provides a valuable framework by connecting turbulence to wave saturation (Hodges, 1967, 1969; R. S. Lindzen, 1981), or applying it thereafter (Holton, 1982; Weinstock, 1982), there are a couple of aspects that might benefit from further refinement: (a) it could lead to an overestimation of turbulence above the saturation altitude, and (b) it doesn't fully capture the turbulence below, which is observed in practice.

We reinterpret the NSP without altering the formalism of R. S. Lindzen (1981) and Holton (1982), but limit its scope. This includes four key points:

1. Turbulence arises from the unstable region caused by the wave's energy release to the mean flow (observed wave-like temperature fluctuations), meaning eddy diffusivity is proportional to the divergence of wave momentum $\left(D_{eddy} \propto \nabla\left(\vec{E}_j\right)\right)$.
2. Therefore, turbulence occurs both below and above the saturation altitude (symmetry).
3. Turbulence limits or eliminates the growth of the influenced region. To prevent excessive temperature gradient growth with altitude during momentum release, the term $|m_r|^{3/2}$ must balance the exponential term $\exp\left[\int_0^z (1/2H - m_i)\, d\zeta\right]$ in 15.
4. At the saturation altitude z_b, the releasing of wave's momentum and the induced turbulence reach their maxima, as the divergence of the EP-flux peaks at z_b (Fritts, 1984; Lott et al., 2012; J. Liu et al., 2023; Yiğit et al., 2008).

Considering the vertical wavenumber definition of (Equation 9) and applying the NSP-(c), one has,

$$\begin{aligned}\frac{1}{|m_r|^{3/2}}\frac{d|m_r|^{3/2}}{dz} &= \frac{3}{2}\frac{1}{m_r}\frac{dm_r}{dz} \\ &= \frac{3}{2}\frac{\Omega}{N|\vec{k}|}\frac{N'|\vec{k}|\Omega - N|\vec{k}|\Omega'}{\Omega^2} \\ &= \frac{3}{2}\left|\frac{1}{N}\frac{\partial N}{dz} - \frac{1}{\Omega}\frac{\partial\Omega}{dz}\right|, \quad z \in [surface, top]\end{aligned} \tag{16}$$

The left side of (Equation 16) is designed to form the term $\ln|m_r|^{3/2}$ when we integrate both sides of the equation. Solving Equation 16 gives the following results:

$$|m_r|^{3/2} = \exp\left[\frac{3}{2}\int_0^z \left|\frac{1}{N}\frac{\partial N}{d\zeta} - \frac{1}{\Omega}\frac{\partial\Omega}{d\zeta}\right| d\zeta\right], \quad \zeta \in [surface, top] \tag{17}$$

The expression in (Equation 17) takes account of the vertical variation of the Brunt-Väisälä frequency N, which has been neglected by R. S. Lindzen (1981) and Holton (1982). The factor cannot be neglected in the upper atmosphere, especially in the region where the saturation is taking place (Hodges, 1967).

To balance the terms in the temperature gradient of (Equation 15) as suggested by NSP-(c), we substitute the $|m_r|^{3/2}$ expression from (Equation 17 into Equation 15), yielding,

$$\Re\left\{\frac{d\delta\hat{T}}{dz}\right\} = -\frac{\Gamma A}{N|\vec{k}|}\exp\left\{\int_0^z \left[\frac{1}{2H} + \frac{3}{2}\left|\frac{1}{N}\frac{\partial N}{\partial\zeta} - \frac{1}{\Omega}\frac{\partial\Omega}{\partial\zeta}\right| - m_i\right] d\zeta\right\}, \quad \zeta \in [surface, top] \tag{18}$$

The jth harmonic gets saturated when the (Equation 18) hits its extrema as implied by NSP-(d). We label the m_i at saturation altitude z_b as $m_{i,s}$, that is, saturated vertical wavenumber of turbulence,

$$\frac{1}{2H}+\frac{3}{2}\left|\frac{1}{N}\frac{\partial N}{\partial z}-\frac{1}{\Omega}\frac{\partial \Omega}{\partial z}\right| = m_{i,s}, \quad z=z_b, \quad \forall j \in [1,M] \tag{19}$$

Note that Equation 19 applies only at the saturation altitude z_b for a given monochromatic wave. R. S. Lindzen (1981) and Holton (1982) extended (Equation 19) to all atmospheric layers above z_b, which is a key difference from our approach.

2.4.3. Saturation of the Wave

As stated in Equation 19 and NSP-(d), the temperature gradient induced by the wave reaches its extrema at the breaking (saturation) altitude z_b. According to NSP-(c), the turbulence triggered by the superadiabatic atmosphere prevents the region from expanding by activating the imaginary part of the vertical wavenumber m_i in (Equation 15), thereby balancing the exponential growth of $\left|\Re\left\{\frac{d\delta\hat{T}}{dz}\right\}\right|$. As a result, $\left|\Re\left\{\frac{d\delta\hat{T}}{dz}\right\}\right|$ should not deviate significantly from the environmental lapse rate Γ due to the induced turbulence. While R. S. Lindzen (1981) proposed that $\left|\Re\left\{\frac{d\delta\hat{T}}{dz}\right\}\right| = \Gamma$ at and above z_b, we argue that this holds only at z_b for a monochromatic wave, as suggested by NSP-(d), providing a constraint to derive the values of A and z_b in Equation 8. Considering the absolute value of the temperature gradient from (Equation 15), we get,

$$\begin{aligned}
&\left|\frac{\Gamma A|m_r|^{3/2}e^{-\int_0^{z_b} m_i d\zeta}e^{z_b/2H}}{N|\vec{k}|}\right| = \Gamma, \quad z=z_b \\
&\frac{\Gamma^2 A^2 m_r^3 e^{-2\int_0^{z_b} m_i d\zeta}e^{z_b/H}}{N^2|\vec{k}|^2} = \Gamma^2, \quad z=z_b \\
&A^2 m_r^{-1}\exp\left(-2\int_0^{z_b} m_i d\zeta\right) = m_r^{-4}N^2|\vec{k}|^2\exp\left(-\int_0^{z_b}\frac{1}{H}d\zeta\right), \quad z=z_b
\end{aligned} \tag{20}$$

Taking into account (Equation 20) and the WKB approximation in (Equation 8), the square of the vertical velocity amplitude $\hat{w}_j$ at the saturation altitude z_b is given by,

$$\begin{aligned}
|\hat{w}_j(z_b)|^2 \approx\ & A^2 m_r^{-1}\exp\left(-2\int_0^{z_b} m_i d\zeta\right) \\
=\ & m_r^{-4}N^2|\vec{k}|^2\exp\left(-\int_0^{z_b}\frac{1}{H}d\zeta\right) \\
=\ & \frac{\Omega^4}{N^2|\vec{k}|^2}\exp\left(-\int_0^{z_b}\frac{1}{H}d\zeta\right)
\end{aligned} \tag{21}$$

The square root of (Equation 21) represents the saturation (breaking) amplitude $\hat{w}_{j,s}$ of a monochromatic wave, initially proposed by R. S. Lindzen (1981). However, Equation 21 assumes the condition of (Equation 20), which enforces a strict non-superadiabatic state around the saturation altitude z_b, meaning no atmospheric turbulence (mixing) is triggered by the saturation. To address this issue, an efficiency factor S_c^2 should be introduced into (Equation 21) to slightly increase the amplitude of $\hat{w}_{j,s}$.

In practice, Lott et al. (2012) provides a version with such an efficiency factor S_c to adjust the amplitude of $\hat{w}_{j,s}$,

$$\hat{w}_{j,s} = \frac{\Omega^2}{|\vec{k}|N}e^{-z/2H}S_c\frac{k^*}{|\vec{k}|}, \quad z=z_b \tag{22}$$

S_c is the saturation parameter and $S_c = 1.5$ for Mars PCM (J. Liu et al., 2023); $k^* = \mathbf{MAX}(|\vec{k}_{\min}|, 1/\sqrt{\Delta x \Delta y})$, a parameter to prevent a monochromatic wave from occupying one whole model grid (De la Cámara et al., 2014). Δx and Δy are the grid intervals of the model (Lott et al., 2012).

To avoid evaluating the saturation altitude z_b directly, we apply the level-to-level WKB approximation of (Equation 10) to $\hat{w}_j$,

$$\hat{w}_j(z_{ll+1}) = \mathbf{MIN}\left\{\hat{w}_j(z_{ll})\sqrt{\frac{m_r(z_{ll})}{m_r(z_{ll+1})}}\exp\left(-\int_{z_{ll}}^{z_{ll+1}} m_i^{ave} d\zeta\right), \hat{w}_{j,s}\right\}, \quad \zeta \in [surface, top] \tag{23}$$

Note that in Equation 22, the vertical index is z instead of z_b. The advantage of this approach is that it allows for the use of the minimum function **MIN** in (Equation 23) to automatically evaluate the vertical evolution of $\hat{w}_j$, rather than specifically imposing $\hat{w}_{j,s}$ at z_b, which is difficult to evaluate directly. Additionally, in Equation 23, the imaginary part im_r^{ave} inside the integral has been omitted compared to (Equation 10).

However, we find a way to evaluate z_b or even A as inspired by (Equation 23). It is useful to determine the value of $\hat{w}_j(z)$ for all $\zeta \in [z_{surface}, z_{top}]$ using (Equation 23). Then, define $\hat{\Pi}_s^2 = |\max(\hat{w}_j(z))|^2 N^2 |\vec{k}|^2/\Omega^4$ and insert it into (Equation 21), yielding,

$$z_b = \log\left(\frac{1}{\hat{\Pi}_s^2}\right)^H \tag{24}$$

By inserting $\hat{\Pi}_s^2$ into (Equation 20) and using Equation 19, we can determine the value of A_j for a monochromatic wave,

$$\begin{aligned} A_j &= |m_r|^{-\frac{3}{2}} N|\vec{k}|\,|\hat{\Pi}_s| \exp\left(\int_0^{z_b} m_i d\zeta\right) \\ &= \frac{z_b}{2H} N|\vec{k}|\,|\hat{\Pi}_s| \\ &= \frac{N|\vec{k}|}{2H}|\hat{\Pi}_s|\log\left(\frac{1}{\hat{\Pi}_s^2}\right)^H \end{aligned} \tag{25}$$

Equations 24 and 25 may provide more accurate estimates for z_b and A compared to other formulas previously proposed. However, these calculations must be performed after obtaining the vertical profiles of each $\hat{w}_j$. Additionally, it is clear that both z_b and A_j are influenced by the wave properties as well as the background atmospheric parameters, such as N^2 and Ω^4.

2.4.4. Critical Layer and Viscosity

The critical layer for a gravity wave is the level where the wave's intrinsic frequency with Doppler shift Ω changes sign,

$$\Theta(\Omega(z_{ll+1}) \times \Omega(z_{ll})) = \begin{cases} 0 & \text{for} \quad \Omega(z_{ll+1}) \times \Omega(z_{ll}) < 0 \\ 1 & \text{for} \quad \Omega(z_{ll+1}) \times \Omega(z_{ll}) \geq 0 \end{cases} \tag{26}$$

The layer forces the wave to release momentum to the mean flow by altering the vertical gradient of the $\hat{w}_j$. The Ω is dominated by background wind $\bar{u}$ for a given wave with horizontal wavenumber $\vec{k}$ and phase velocity c. Thus, these layers have a strong "filtering" effect on the wave (J. Liu et al., 2023, 2025; Roeten et al., 2022). The critical layer is applied by multiplying (Equations 23–26),

$$\hat{w}_j(z_{ll+1}) = \Theta[\Omega(z_{ll+1}) \times \Omega(z_{ll})]\,\mathbf{MIN}\left\{\hat{w}_j(z_{ll})\sqrt{\frac{m_r(z_{ll})}{m_r(z_{ll+1})}}\exp\left(-\int_{z_{ll}}^{z_{ll+1}} m_i^{ave}\,d\zeta\right), \hat{w}_{j,s}\right\} \tag{27}$$

The advantage of this critical layer setting is to force the monochromatic wave's amplitude to zero at the critical layer without interrupting the propagation of a wave ensemble (which includes several monochromatic waves). The induced ensemble $\hat{w}$ damps a bit at each critical layer and keeps propagating to higher altitudes.

As the wave goes upwards, the atmospheric viscosity serves as a key factor that damps the $\hat{w}$ (Fritts, 1984; Lott et al., 2012). We assume the kinematic viscosity ν increases with altitude due to the decrease of the atmospheric mass density such as $\nu = \mu/\rho$ (Lott et al., 2012). Additionally, Lott et al. (2012) takes $m_i^{ave} \approx D_{eddy}^j m_r^3/\Omega$ and absorbs D_{eddy}^j into the dynamical viscosity μ, making the $\mu^* = \mu D_{eddy}^j$ a tunable parameter (such as $\mu^* \approx 0.07$ in Mars PCM). It returns,

$$\hat{w}_j(z_{ll+1}) = \underbrace{\Theta[\Omega(z_{ll+1})\Omega(z_{ll})]}_{\mathbf{CL}}\mathbf{MIN}\left\{\hat{w}_j(z_{ll})\sqrt{\frac{m(z_{ll})}{m(z_{ll+1})}}\exp\left(-\underbrace{\frac{\mu^*}{\rho}}_{\mathbf{VD}}\overbrace{\frac{m_r^3}{\Omega}}^{\mathbf{TD}}\delta z\right), \underbrace{\hat{w}_{j,s}}_{\mathbf{ST}}\right\} \tag{28}$$

Equation 28 represents the non-orographic GWs induced amplitude of the vertical velocity $\hat{w}_j$ in a complete form. The critical layers (**CL**), saturation (**ST**), kinematic viscosity (**VD**), and (GW-induced) turbulence damping (**TD**) are considered together in terms of WKB approximation of $\hat{w}_j$. The variables of this equation are all known parameters of a given wave or background atmosphere. The term **TD** is detailed in Section 3.1.2. It is convenient to apply (Equation 28 into Equation 3) to evaluate the vertical evolution of the wave's EP-flux.

2.5. Evolution of the EP-Flux

We launch the waves at the average top of the planetary boundary layer. Inserting the complete WKB approximation of $\hat{w}_j$ (Equation 28) into the EP-flux definition of (Equation 3) and letting the EP-flux evolution in the direction of $\vec{k}\Omega/|\vec{k}\Omega|$, yields,

$$\vec{E}_j^{z_{ll+1}} = \frac{\vec{k}\Omega}{|\vec{k}||\Omega|}\Theta[\Omega(z_{ll+1})\Omega(z_{ll})]\,\mathbf{MIN}\left\{|\vec{E}_j^{z_{ll}}|e^{-2\frac{\mu^* m^3}{\rho\Omega}\delta z}, \rho_r S_c^2 e^{-\frac{z_{ave}}{H}}\frac{|\Omega|^3 k^{*2}}{2N|\vec{k}|^4}\right\} \tag{29}$$

We update the EP-flux by iteration loop from layer z_{ll} to z_{ll+1}, in which $\delta z = z_{ll+1} - z_{ll}$ and $z_{ave} = (z_{ll} + z_{ll+1})/2$, respectively. The EP-flux at the reference altitude $\vec{E}_j^{z_r}$ is sampled from a normal distribution with a maximum truncation value of 5×10^{-4} kg m^{-1} s^{-2} (J. Liu et al., 2023).

2.6. Divergence of the EP-Flux

The drag caused by the waves is given by $\partial\vec{u}/\partial t = -\rho^{-1}d\vec{E}/dz$. The drag of a wave ensemble with M =8 monochromatic waves is evaluated by the average drag of all waves. We use first-order Auto Regression (AR1) to average the drags on the winds and update the winds' tendencies between physical time steps t and $t + \delta t$ by (Lott et al., 2012; Lott & Guez, 2013):

$$\left(\frac{\partial\vec{u}}{\partial t}\right)_{GW}^{t+\delta t} = \frac{\delta t}{\Delta t}\frac{1}{M}\sum_{j=1}^{M}\frac{1}{\rho}\frac{d\vec{E}_j}{dz} + \frac{\Delta t - \delta t}{\Delta t}\left(\frac{\partial\vec{u}}{\partial t}\right)_{GW}^{t} \tag{30}$$

Thus we have $C_j^2 = \left(\frac{\Delta t - \delta t}{\Delta t}\right)^p \frac{\delta t}{M\Delta t}$, where $p = \lfloor (j-1)/M \rfloor$ is an integer. Δt is the life cycle of the non-orographic gravity waves, which is approximately 24 hr or 1 sol (Lott et al., 2012). Note that the gravity waves' entire spectrum is accumulated over the typical life cycle of the waves Δt, which means that about $M\Delta t/\delta t$ harmonics are ejected, a number that easily is on the order of 10^3. This excellent spectral resolution at a small

numerical cost ($M = 8$ waves are quite fast to evaluate each δt) is one of the benefits of the scheme. It is worth noticing that there is no temperature tendency to be implemented in the scheme. We expect that the temperature changes can be captured by the Mars PCM energy conservation design.

3. Turbulence Induced by the Non-Orographic Gravity Waves

This section derives the eddy diffusion coefficient. It represents turbulence triggered at different altitudes. The method follows the NSP, linear damping assumption, and empirical analysis. We derive the eddy diffusivity D_{eddy} proposed by R. S. Lindzen (1981). It is valid primarily at the saturation altitude z_b for a given monochromatic wave, as indicated by NSP-(d). The formulations by Holton (1982) and Weinstock (1982) may apply above z_b, consistent with NSP-(a) and NSP-(c). Below z_b, we adopt an exponential decay of eddy diffusivity based on retrievals from tracer's number density n_q, assuming 'symmetric turbulence' around z_b (NSP-(b)), where $D_{eddy} \propto 1/\sqrt{n_q}$ (Rodrigo et al., 1990). The turbulent flux from each wave ensemble is averaged over $M = 8$ monochromatic waves and incorporated into the model tendency via an AR-1 process.

3.1. Eddy Diffusion Coefficient

3.1.1. Linear Damping Assumption

The effect of GW-induced eddy diffusion is approximated by linear damping at and above the saturation altitude (Holton, 1982; R. S. Lindzen, 1981). Assuming that diffusion contributes as a dissipation term in the equations for energy and momentum, we have,

$$D^j_{eddy}\frac{\partial}{\partial z^2}\begin{Bmatrix}\widehat{\bar{u}}\\ \delta\hat{T}\end{Bmatrix} = -m_r^2 D^j_{thermal}\begin{Bmatrix}\widehat{\bar{u}}\\ \delta\hat{T}\end{Bmatrix}, \quad z \geq z_b \tag{31}$$

where we assume the Prandtl number $\mathrm{Pr} = D^j_{eddy}/D^j_{thermal} = 1$. Although this assumption may be too small compared to 4 or 6 as suggested by Strobel et al. (1985) and Barnes et al. (1996), the constant can be treated as a tunable parameter in practical implementation (Fritts & Alexander, 2003).

Equation 31 implies that a quantity of $m_r^2 D^j_{eddy}$ has contributed to the system. Consequently, the thermodynamic energy equation of (Equation 11) for jth monochromatic harmonic becomes,

$$\left[i\vec{k}(c-\bar{u}) + m_r^2 D^j_{eddy}\right]\delta\hat{T} = \hat{w}_j e^{z/2H}\Gamma, \quad z \geq z_b \tag{32}$$

The term $m_r^2 D^j_{eddy}$ must be eliminated in (Equation 32) by turbulence (NSP-(c)) to keep the same form as (Equation 11). This is equivalent to introducing an imaginary part of wave phase velocity, $c_i = \Im(c)$, to balance the term $m_r^2 D^j_{eddy}$ (Holton, 1982). Hence, corresponding to $m = m_r + im_i$, we rewrite $c = c_r + ic_i$. Inserting this c into (Equation 32), we know that the extra heating rate contributed by the wave is balanced by the turbulence using c_i,

$$\vec{k}c_i\delta\hat{T} = m_r^2 D^j_{eddy}\delta\hat{T}, z \geq z_b \tag{33}$$

It is convenient to use (Equation 33) to evaluate the D^j_{eddy}, that is, $D^j_{eddy} = \vec{k}c_i/m_r^2$. However, the value of c_i is unknown. Therefore, we need to find the relationship between c_i and m_i and express D^j_{eddy} in terms of m_i. Either m_i or c_i represents the turbulence, and we may refer to c_i as the phase velocity of turbulence.

3.1.2. m_i and c_i

Assuming that the vertical wavenumber m has an overall form similar to its real part as shown in (Equation 9). The connection between m and c is through the parameter $\Omega = \vec{k}\left(\frac{\vec{k}}{|\vec{k}|}c - \vec{\bar{u}}\right)$, the wave's intrinsic frequency with

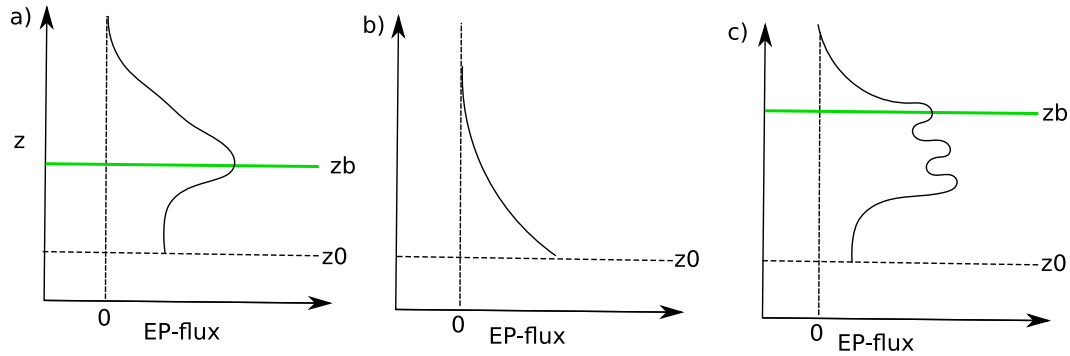

Figure 1. Wave saturation altitudes for three basic forms. (a) Normal case: z_b at the altitudes where maximum of EP-flux take place; (b) $z_b = z_0$, the wave breaks once it is launched; (c) z_b at the upper most saturation levels.

Doppler shift. R. S. Lindzen (1981) proposed to apply $c = c_r + ic_i \left(i^2 = -1\right)$ to m to derive the m_i by using the relation provided in (Equation 33). It follows,

$$\begin{aligned} m &= \frac{N|\vec{k}|}{\vec{k}\left(\vec{u} - \vec{k}/|\vec{k}|c\right)} \\ &= \frac{N|\vec{k}|}{\vec{k}\left(\vec{u} - \vec{k}/|\vec{k}|c_r\right) - im_r^2 D_{eddy}^j} \\ &= -\frac{N|\vec{k}|\Omega}{\Omega^2 + m_r^4 D_{eddy}^2} + i\frac{N|\vec{k}|m_r^2 D_{eddy}^j}{\Omega^2 + m_r^4 D_{eddy}^2}, \quad z \geq z_b \end{aligned} \tag{34}$$

where the term $m_r^4\left(D_{eddy}^j\right)^2$ in (Equation 34) is the turbulence contribution to the vertical wavenumber m. Additionally, the typical vertical wavelength of gravity waves is 15 km ($m_r = 2\pi/15 \times 10^{-3} \approx 5 \times 10^{-4}$ m^{-1}) and the D_{eddy}^j is at 10^6 cm^2 s^{-1}, which makes the term $m_r^4 D_{eddy}^2 \approx 10^{-10}$ s^{-2} $\ll \Omega^2$. This implies the term $m_r^4 D_{eddy}^2$ is negligible. Unsurprisingly, now the first term of (Equation 34) is $-N|\vec{k}|/\Omega$, which is the exact definition of m_r in (Equation 9). By the same reasoning, we can conclude that the second term (the imaginary part) equals m_i, reads,

$$m_i = \frac{N|\vec{k}|m_r^2 D_{eddy}^j}{\Omega^2}, \quad z \geq z_b \tag{35}$$

Equation 35 shows the efficiency of turbulence arising from the superadiabatic thin layers at $z \geq z_b$. Additionally, Equation 35 explains why Lott et al. (2012) takes $m_i^{ave} \approx m_r^3/\Omega D_{eddy}^j$ in (Equation 28). The linear damping may not be accurate for the waves with short vertical wavelengths less than 10 km (Figure 1 of Hodges (1969)), which break mostly in the lower atmosphere. Applying (Equation 35) below z_b needs to introduce a tunable parameter such as the one in Lott et al. (2012).

3.1.3. Saturated Eddy Diffusivity

The m_i must take a specific value at the altitude of z_b as indicated by NSP-(d). The m_i in (Equation 35) equals the $m_{i,s}$ of (Equation 19) at z_b,

$$\frac{N|\vec{k}|m_r^2 D_{s,eddy}^j}{\Omega^2} = \frac{3}{2}\left|\frac{1}{N}\frac{dN}{dz} - \frac{1}{\Omega}\frac{d\Omega}{dz}\right| + \frac{1}{2H}, \quad z = z_b \tag{36}$$

Note that (Equation 36) holds only at the saturation altitude for jth wave, in which we have applied the NSP-(c) and (d) to the thermodynamic equations to limit the enlargement of the "unstable" region (where the turbulence comes from). Therefore, the saturated eddy diffusivity $D^j_{s,eddy}$ inferred from (Equation 36) is as,

$$D^j_{s,eddy} = \frac{\Omega^4}{N^3|\vec{k}|^3}\left(\frac{3}{2}\left|\frac{1}{N}\frac{dN}{dz} - \frac{1}{\Omega}\frac{d\Omega}{dz}\right| + \frac{1}{2H}\right), \quad z = z_b, j \in [1, M] \tag{37}$$

For the same reason, Equation 37 is only effective at the saturated altitude z_b for a monochromatic wave. A limitation arises in R. S. Lindzen (1981), where Equation 37 is applied throughout the atmosphere above z_b. This approach does not account for the fact that the $m_{i,s}$ relationship in (Equation 19) represents an extremum condition as indicated by NSP-(d), which is strictly valid only for saturated monochromatic waves at z_b.

Analogous to the concept of saturation amplitude of the EP-flux of (Equation 22) provided by Lott et al. (2012), we propose Equation 37 as "saturated eddy diffusivity" by giving it a tunable parameter,

$$D^j_{s,eddy} = S_{mix}\frac{\Omega^4}{N^3|\vec{k}|^3}\left(\frac{3}{2}\left|\frac{1}{N}\frac{dN}{dz} - \frac{1}{\Omega}\frac{d\Omega}{dz}\right| + \frac{1}{2H}\right) \quad z = z_b, j \in [1, M] \tag{38}$$

Where S_{mix} is a constant with a magnitude of 0.1. Equation 38 indicates that the saturated eddy diffusivity of a given wave is proportional to $m_{s,i}$. This equation has a "symmetric" $m_{s,i}$ that includes the perturbations of the background atmosphere Brunt-Väisälä frequency, which makes the formula more suitable for application in the upper atmosphere (Hodges Jr, 1967, 1969). Note that both (Equations 35 and 38) imply $D^j_{eddy} \propto m_r^{-3} \propto \lambda_z^3$, which waves with longer wavelength λ_z provide stronger mixing. This is introduced mainly due to the linear damping assumption.

3.1.4. Eddy Diffusivity Above z_b

We expect the wave momentum to be released intensively once it achieves saturation, as mentioned before. This is true, as shown in J. Liu et al. (2023). This implies that the induced turbulence should also hit its maximum along with the saturation (NSP-d) and evolve with the damping of the momentum at higher altitudes (NSP-a). According to NSP-a that turbulence $\propto \nabla \vec{E}_j$, it prompts us to work toward establishing a relationship between D^j_{eddy} and the EP-flux $\vec{E}_j$.

However, the eddy diffusivity of the upper atmosphere derived from observations (Rodrigo et al., 1990) shows that there are still 10^5 to 10^7 cm^2 s^{-1} mixing excited above the turbopause or even above the exobase. We would like to point out that this mixing should not be attributed to gravity waves, since the EP-flux decays so fast after the saturation that it could cause any observable turbulence. This suggests that the molecular diffusion dominates above the turbopause (Slipski et al., 2018).

The original algorithm to build up the connections between D^j_{eddy} and the wave's EP-flux is proposed by Holton (1982) and Weinstock (1982). Here we follow similar formalisms, but the derivations are based on the NSP and linear damping assumptions.

We start with the EP-flux definition of (Equation 3). By inserting the WKB solution of (Equation 8) into (Equation 3), and using the $A^2 - z_b$ relation of (Equation 20), the EP-flux integral function with independent variable z reads,

$$
\begin{aligned}
\vec{E}_j^z &= -\rho \frac{\vec{k}}{2|\vec{k}|^2} m_r |\hat{w}_j|^2 \\
&= -\rho \frac{\vec{k}}{2|\vec{k}|^2} A^2 e^{-2\int_0^z m_i d\zeta} \\
&= -\rho \frac{\vec{k}}{2|\vec{k}|^2} A^2 e^{-2\int_0^{z_b} m_i d\zeta} e^{-2\int_{z_b}^z m_i d\zeta} \\
&= \rho \frac{\Omega^3}{2N|\vec{k}|^2} \frac{\vec{k}}{|\vec{k}|} e^{-\int_0^{z_b} \frac{1}{H} d\zeta} e^{-2\int_{z_b}^z m_i d\zeta}, \quad \zeta \in [surface, top]
\end{aligned} \tag{39}
$$

The term $\exp\ -2\int_{z_b}^z m_i d\zeta$ in Equation 39 is contributed by turbulence damping above z_b. As mentioned in Sections 2.4.1–2.4.3, we rely on m_i to regulate the amplitude of the turbulence. We expect m_i to do the same above the saturation altitude z_b. The drag caused by the wave's momentum release above z_b follows,

$$
\begin{aligned}
-\frac{1}{\rho}\frac{\partial \vec{E}_j^z}{\partial z} &= -\frac{\partial}{\partial z}\left(\frac{\Omega^3}{2N|\vec{k}|^2} e^{-\int_0^{z_b} \frac{1}{H} d\zeta} e^{-2\int_{z_b}^z m_i d\zeta} \right) \\
&= m_i \frac{\Omega^3}{N|\vec{k}|^2} e^{-\int_0^{z_b} \frac{1}{H} d\zeta} e^{-2\int_{z_b}^z m_i d\zeta}, \quad \zeta \in [surface, top]
\end{aligned} \tag{40}
$$

Here $\vec{k}/|\vec{k}|$ drops since the derivation takes along z.

We apply $m_i = D_{eddy}^j m_r^3/\Omega$ for the m_i in (Equation 40) to consider the evolution of the divergence of the EP-flux above z_b. It follows,

$$
D_{eddy}^j = \frac{\Omega}{N^2|\vec{k}|}\left\{ -\frac{1}{\rho}\frac{\partial \vec{E}_j^z}{\partial z} \right\} e^{\int_0^{z_b} \frac{1}{H} d\zeta} e^{2\int_{z_b}^z m_i d\zeta}, \quad z \geq z_b \tag{41}
$$

Here we have applied the linear damping assumption, therefore, (Equation 41) holds at $z \geq z_b$. The last two exponential terms of (Equation 41) should be considered as a constant for convenience. We shape the terms into a tunable parameter called α_{eff},

$$
\begin{aligned}
\alpha_{eff} &= e^{\int_0^{z_b} \frac{1}{H} d\zeta} e^{2\int_{z_b}^z m_i d\zeta} \\
&= \exp\left(-\frac{z}{H} + 3\left| \frac{1}{N}\frac{\partial N}{dz} - \frac{1}{\Omega}\frac{\partial \Omega}{dz} \right|_{z_b}^z \right) \\
&\approx \exp\left(-\frac{z - z_b}{H} \right), \quad z \geq z_b
\end{aligned} \tag{42}
$$

The wave's depletion altitudes are always 20–40 km above its saturation altitude. Here the term $\exp[-(z - z_b)/H]$ forms a factor α_{eff} between 0.01 $\left(e^{-4}\right)$ to 0.2 $\left(e^{-2}\right)$. The factor indicates the distance effect between z_b and the altitudes above. It is worth noticing that we partially applied the $m_{i,s}$ at z_b directly into the altitudes above. This bold action was first made by Holton (1982). Our best explanation for this is that we consider the variation of m_i in altitudes to be linear since it is a slowly changing parameter. The influence has been absorbed by the term α_{eff},

$$
D_{eddy}^j = \alpha_{eff} \frac{\Omega}{N^2|\vec{k}|}\left\{ -\frac{1}{\rho}\frac{\partial \vec{E}_j^z}{\partial z} \right\}, \qquad z \geq z_b \tag{43}
$$

In addition, (Equation 43) can be achieved by inserting $m_{i,s}$ into (Equation 41) in both terms. This implies that the NSP-d constraint $|\Re(d\delta\hat{T}/dt)| = \Gamma$ and the linear damping assumption in (Equation 31) share similarities at altitudes $z \geq z_b$.

Since "saturation" and "linear damping" have been introduced to the derivation, which leads $D^j_{eddy} \propto m_r^{-3} \propto \lambda_z^3$. The relation in (Equation 43) favors the middle-upper atmosphere since waves with longer wavelengths break at higher altitudes. Meanwhile, the eddy diffusivity will be underestimated at the lower atmosphere where the breaking of short wavelength waves takes place. Therefore, (Equation 43) is suitable for levels above the wave's saturation altitude.

3.1.5. Eddy Diffusivity Below z_b

The assumption of turbulence triggered by wave saturation would lack the capability to predict mixing below z_b. Therefore, we have to change the concepts of the NSP as mentioned before. Here we focus on the NSP-a and NSP-b. In other words, we assume if there is momentum released from the wave, there is turbulence generated; otherwise, no turbulence. This assumption is generally true since we have observed wave-induced eddy diffusivity both below and above the saturation altitude from observations (Anderson & Leovy, 1978; M. B. McElroy & Donahue, 1972; Nier & McElroy, 1976; Rosenqvist & Chassefière, 1995; Shimazaki, 1989; Sprague et al., 2004; Slipski et al., 2018; Yoshida et al., 2022).

Now, the problem is how to evaluate the eddy diffusion coefficient below the wave's breaking altitude. It has been confirmed by many observations that the coefficient follows a power law to the long-existed tracers' abundances below the upper atmosphere (Von Zahn et al., 1980; Yoshida et al., 2022),

$$D^j_{eddy} = \mathcal{B} \times n_q^{-1/2} \tag{44}$$

where $\mathcal{B}$ is a constant of magnitude of 10^{13} to 10^{14} (Rodrigo et al., 1990; Yoshida et al., 2022); n_q is the number density (in cm^{-3}) of the tracer q. We always assume the density $n \propto \exp\left(-\frac{z}{H}\right)$. Equation 44 indicates a monotonically growing eddy diffusion coefficient that is proportional to $e^{z/H}$ below z_b. It equals the saturated eddy diffusivity at z_b. It is not very hard to guess that Equation 44 is equivalent to (Garcia & Solomon, 1985; Holton, 1982, 1983),

$$D^j_{eddy} = D^j_{eddy}(z_b)\, e^{\beta_{diff}(z-z_b)/H}, \qquad z < z_b \tag{45}$$

where β_{diff} is a positive constant that represents the growth rate of the diffusion coefficient. It turns out that $\beta_{diff} = 1.5$ (Garcia & Solomon, 1985). This equation is a purely empirical relationship derived from observations (Yoshida et al., 2022). However, it fully satisfies NSP-a and NSP-b. The drag in below does decrease exponentially from its peaks at saturation level (J. Liu et al., 2023). In other words, Equation 45 reveals the same nature as (Equation 43): the turbulence triggered by the wave is proportional to the wave's divergence of the momentum (NSP-a).

3.1.6. A Comprehensive Formula

A comprehensive formula of the eddy diffusion coefficient D^j_{eddy} of jth monochromatic harmonic for the whole atmosphere can be given by combining (Equations 38, 43, and 45),

$$D^j_{eddy} = \begin{cases} \mathbf{MIN}\left[\alpha_{eff}\dfrac{\Omega}{N^2|\vec{k}|}\left(-\dfrac{1}{\rho}\dfrac{\partial\vec{E}}{\partial z}\right),\quad S_{mix}\dfrac{\Omega^4}{N^3|\vec{k}|^3}\left(\dfrac{3}{2}\left|\dfrac{1}{N}\dfrac{dN}{dz} - \dfrac{1}{\Omega}\dfrac{d\Omega}{dz}\right| + \dfrac{1}{2H}\right)\right] & \text{for} \quad z \geq z_b \\ D^j_{eddy}(z_b)\exp\left[\beta_{diff}\dfrac{(z-z_b)}{H}\right] & \text{for} \quad z < z_b \end{cases} \tag{46}$$

Here we have three tunable parameters: the effective mixing factor $\alpha_{eff} = 0.1$ (Imamura et al., 2016); the saturated factor of mixing $S_{mix} = 0.1$; and diffusion decrease rate $\beta_{diff} = 1.5$ (Garcia & Solomon, 1985).

Equation 46 continues at altitude z_b with eddy diffusivity $D^j_{eddy}(z_b)$. The comprehensive formula makes sure the wave-induced mixing reaches its maximum at z_b (NSP-d) and decreases with the divergence of the wave's momentum above (NSP-a). The mixing decreases from $D^j_{eddy}(z_b)$ at altitudes below (NSP-a). In addition, it is convenient to evaluate the divergence of the wave's momentum above z_b since the EP-flux has been treated in the non-orographic GWs schemes as shown in (Equation 28).

3.2. Diffusion Flux

Assuming that the diffusion occurs along the "propagation path" $\left(\text{i.e., in the direction of } \frac{\vec{k}\Omega}{|\vec{k}\Omega|}\right)$ of the wave, the diffusion flux $\Phi^{df\,\bar{u}}_j$ for the mean zonal flow $\bar{u}$ associated with a monochromatic wave j thus can be expressed as,

$$\Phi^{df\,\bar{u}}_j = \rho \frac{\vec{k}\Omega}{|\vec{k}||\Omega|} D^j_{eddy} \frac{\partial \bar{u}}{\partial z} \tag{47}$$

Note that only the zonal diffusion flux has been implemented, corresponding to the non-orographic gravity wave's EP-flux (Lott et al., 2012; Lott & Guez, 2013; J. Liu et al., 2023). Here the minus sign in front ρ is omitted, as the corresponding tendency equation already includes a minus sign in front of $1/\rho$; ρ the background atmospheric mass density. The operator $\rho D^j_{eddy}\partial/\partial z$ turns the diffusion into momentum flux for a given field such as zonal wind.

This diffusion process also results in a mixing flux for the potential temperature θ, given by

$$\Phi^{df\,\theta}_j = \rho \frac{\vec{k}\Omega}{|\vec{k}||\Omega|} D^j_{eddy} \frac{\partial \theta}{\partial z} \tag{48}$$

We expect that the atmosphere parcels involved in this mixing rise or descend adiabatically, without including significant instability in the potential temperature profile. Thus, the superadiabatic region where the turbulence comes from is stabilized and will not expand further by applying (Equation 48).

The tracers are assumed to be mixed by the turbulence. The mixing flux for a given tracer q_k is similarly described by,

$$\Phi^{df\,q_k}_j = \rho \frac{\vec{k}\Omega}{|\vec{k}||\Omega|} D^j_{eddy} \frac{\partial q_k}{\partial z} \tag{49}$$

Here the term $\rho \frac{\vec{k}\Omega}{|\vec{k}||\Omega|}\left(\frac{q_k}{T}\frac{\partial T}{\partial z} + \frac{q_k}{H}\right)$ (Rodrigo et al., 1990) is neglected due to its value being significantly smaller than that of $\Phi^{df\,q_k}_j$ in Equation 49. More complex mixing implementation, taking into account factors such as the density gradient of tracers, especially for non-Lagrangian tracers, will be considered in a dedicated paper. In total, 43 tracers are mixed by this scheme within the Mars PCM model. The turbulence is expected to change the tracers' concentrations instantaneously. The impacts on the chemical cycle of the atmosphere will be handled by advanced chemical modules in Mars PCM.

3.3. Turbulence Mixing

The diffusion flux $\Phi^{df\,\bar{u}}_j$ can trigger zonal wind tendency since (Equation 47) is equivalent to momentum flux as mentioned before. The tendency is added to the mean flows using an AR-1 algorithm similar to Equation 30,

$$\left(\frac{\partial \vec{u}}{\partial t}\right)^{t+\delta t}_{mix} = \frac{\delta t}{\Delta t}\frac{1}{M}\sum_{j=1}^{M}\frac{1}{\rho}\frac{d\Phi^{df\,\bar{u}}_i}{dz} + \frac{\Delta t - \delta t}{\Delta t}\left(\frac{\partial \vec{u}}{\partial t}\right)^{t}_{mix} \tag{50}$$

Here the tendency is only implemented in the zonal flow same as Equation 30. Note that this "drag" is induced by non-orographic GWs' turbulence. The "drag" in (Equation 30) is triggered by non-orographic GWs. The maximum magnitudes of turbulence-caused drags are only 10%–20% or even smaller than non-orographic GWs-induced drags.

Similarly, the mixing to the potential temperature θ is,

$$\left(\frac{\partial\theta}{\partial t}\right)_{mix}^{t+\delta t} = \frac{\delta t}{\Delta t}\frac{1}{M}\sum_{j=1}^{M}\frac{1}{\rho}\frac{d\Phi_i^{df\theta}}{dz} + \frac{\Delta t-\delta t}{\Delta t}\left(\frac{\partial\theta}{\partial t}\right)_{mix}^{t} \tag{51}$$

The background atmosphere can keep "stable" stats by applying AR-1 to the mixing-induced zonal wind and potential temperature tendency.

Two types of implementation of mixing to the tracers have been tested. (a) The impacts to the tracers q_k by turbulence can be applied instantaneously, yielding,

$$\frac{\partial q_k}{\partial t} = \frac{1}{M}\sum_{j=1}^{M}\frac{1}{\rho}\frac{d\Phi_i^{dfq_k}}{dz} \tag{52}$$

Or (b) we apply the AR-1 average over $\Delta t = 1$ sol, read,

$$\left(\frac{\partial q_k}{\partial t}\right)_{mix}^{t+\delta t} = \frac{\delta t}{\Delta t}\frac{1}{M}\sum_{j=1}^{M}\frac{1}{\rho}\frac{d\Phi_i^{dfq_k}}{dz} + \frac{\Delta t-\delta t}{\Delta t}\left(\frac{\partial q_k}{\partial t}\right)_{mix}^{t} \tag{53}$$

The test simulations show that the two types of implementations have similar impacts on the model's temperature and densities. We expect the tracers to be mixed by the turbulence, that is, bumping up and down (determined by the waves' path vector $\vec{k}\Omega/|\vec{k}\Omega|$) in a steady atmosphere. At the same time, the model's chemical-photochemical scheme and other dynamics-related modules could take care of the tracers' reactions and trajectories.

3.4. The Saturation Altitude

We can achieve an analytical form of wave saturation altitude z_b from Equation 20 as done by R. S. Lindzen (1981) and Holton (1982). However, the analytical equation is not practical because it includes the unknown constant A^2. Thus, we have to look into the maximum of Equation 5 to search for the z_b. The scheme launched a wave ensemble that includes $M = 8$ monochromatic waves at each time step at a given location. Each of the monochromatic waves has one of three basic EP-flux forms as shown in Figure 1.

Most of the monochromatic waves have a single peak as illustrated in Figure 1a, in which the saturation altitude is located where the EP-flux takes its maximum value. The second form of wave (Figure 1b) depletes fast above its launch level z_0. Thus, the saturation altitude is at the launch altitude ($z_0 = z_b$). In some extremely rare cases, the harmonic breaks a few times after the saturation peak (Figure 1c). There are 2–5 levels between the first saturation (EP-flux maximum) and the final breaking level. In such a case, we take the last breaking level as the z_b to avoid negative values (due to the derivative along z) when using Equation 43 to evaluate the D_{eddy}^{j}. Therefore, the $D_{eddy}^{j}(z_b)$ for this type of monochromatic wave has been underestimated. Again, this effect can be balanced by the **MIN** function in (Equation 46) and the tunable parameters.

4. Sensitive Tests With Mars PCM

The tests of the non-orographic gravity waves scheme on the Mars Planetary Climate Model have been done by J. Liu et al. (2023). The results show that the model simulations with the scheme turned on successfully recovered the temperature/tide structures observed by the Mars Climate Sounder (MCS) below 100 km. Additionally, the high-altitude cold pockets presented in the MCS measurements (Heavens et al., 2022) are recovered by the model and explained directly for the first time. Furthermore, the simulated results are compatible with the NGIMS-derived densities in the upper atmosphere.

The impacts of non-orographic GW on the Martian atmosphere are significant during a whole Mars Year (J. Liu et al., 2023; J. Liu et al., 2025). Here we may only focus on demonstrating the differences between the clean-sky (Ls 60°-90°) and dusty season (Ls 240°-270°) for convenience. Detailed discussions for other periods may need dedicated papers.

The sensitive tests presented here compare the observations with the model simulations that include three types of modes: gravity waves off (GWoff), gravity waves on (GWon), and gravity waves mixing on (GWon + mixing; the mixing scheme is only available when the gravity wave scheme is turned on). The mixing scheme proposed above has now been adopted as one of the main physical packages in Mars PCM.

4.1. Model Configuration

The Mars Planetary Climate Model (formally known as LMD Mars GCM) has a grid resolution of $64 \times 48 \times 73$ that represents an average horizontal resolution of $5.625° \times 3.75°$ (longitude × latitude) and pseudo-altitudes from the model surface up to 250 km. The model has been coupled to an extended LMDZ physics package to simulate multiple atmospheric processes from the sub-surface layer to the exosphere. A configuration of MCD6.0-like (the most complete and advanced one) has been set up for the tests discussed in this paper (J. Liu & Millour, 2025). We tend not to describe what an MCD6.0-like configuration is here, since it might include a couple of dedicated papers to explain. However, we do select the Mars Years (MY29-MY36) to do the simulations. This is because there are multiple observations to compare to during MY29-MY36. Second, there are some realistic and high-quality measurement-retrieved scenarios (such as dust storms, water cycle, and solar inputs) during these MYs. A total of $k = 43$ tracers (q_k) have been used in the model.

4.2. Results and Analysis

4.2.1. Model Simulated D_{eddy}

The eddy diffusion coefficients are co-located with the drags of the non-orographic drags (Figure 2). Three maximums exist in latitudes and in altitudes between 10^0 to 10^{-4} Pa during the clear-sky seasons (Figure 2a), which correspond to the three momentum release spots (Figure 2c). The maximums of D_{eddy} unfold as a humpbacked structure in altitudes during dusty seasons (Figure 2b), corresponding to the double drags peaks induced by the saturated waves (Figure 2d). The distribution of D_{eddy} in altitude-latitude space is not a surprise since the coefficient is designed to be a ratio to the momentum release as shown in Equation 46.

The coefficient lies between 10^3 and 10^5 cm^2 s^{-1} below 10^0 Pa ($\approx$ 60 km) and hits maximums of 10^6 to 10^7 cm^2 s^{-1} above during Ls 60°-90°(Figure 2a). The diffusivity approaches zero quickly above 10^{-4} Pa ($\approx$140 km) where the waves' momentum is exhausted (Figure 2c). There are minor mixing regions with diffusivity of 0 to 10^3 cm^2 s^{-1} lying among the gaps of the drags distribution. These minima in drags are caused by the "filtering effect" due to slow background winds at lower altitudes in the corresponding latitudes (J. Liu et al., 2023, 2025). These deep decreases and latitudinal variations in D_{eddy} are consistent with derivations from NGIMS (Jakosky et al., 2017; Slipski et al., 2018).

The dusty seasons have larger D_{eddy} of magnitudes of 10^6 to 10^8 (or even 10^9) cm^2 s^{-1} above 10^{-1} Pa ($\approx$ 80 km) (Figure 2b). A much smoother distribution of diffusivity of magnitudes of 10^3 and 10^5 cm^2 s^{-1} than the clear-sky seasons (Figure 2a) lies below. Meanwhile, a deeper minor mixing region with diffusivity less than 10^3 cm^2 s^{-1} appears between 6°S and 16°N at altitudes above 10^0 Pa, relating to the minimums of the waves' activities (Figure 2d). Additionally, the humpbacked distribution of the coefficient in the upper atmosphere makes the waves-induced turbulence extend to higher altitudes (160–180 km) during the dusty seasons than the ones (130–150 km) during clear-sky seasons.

Figure 2 indicates a highly uneven turbopause in altitude-latitude space, which evolves seasonally. The turbopause is the boundary above which the diffusivity is dominated by molecular diffusion or the boundary where the non-orographic GWs-induced mixing is exhausted. Thus, the boundary varies between 100 and 140 km during Ls 60°-90° (Figure 2a) and oscillates between 80 and 160 km dependent on latitudes during dusty seasons (Figure 2b). It is due to the enhanced intensities and saturation altitudes of the waves caused by the dust storms (J. Liu et al., 2019, 2023; Roeten et al., 2022; Yiğit et al., 2015, 2021; Yiğit, 2021).

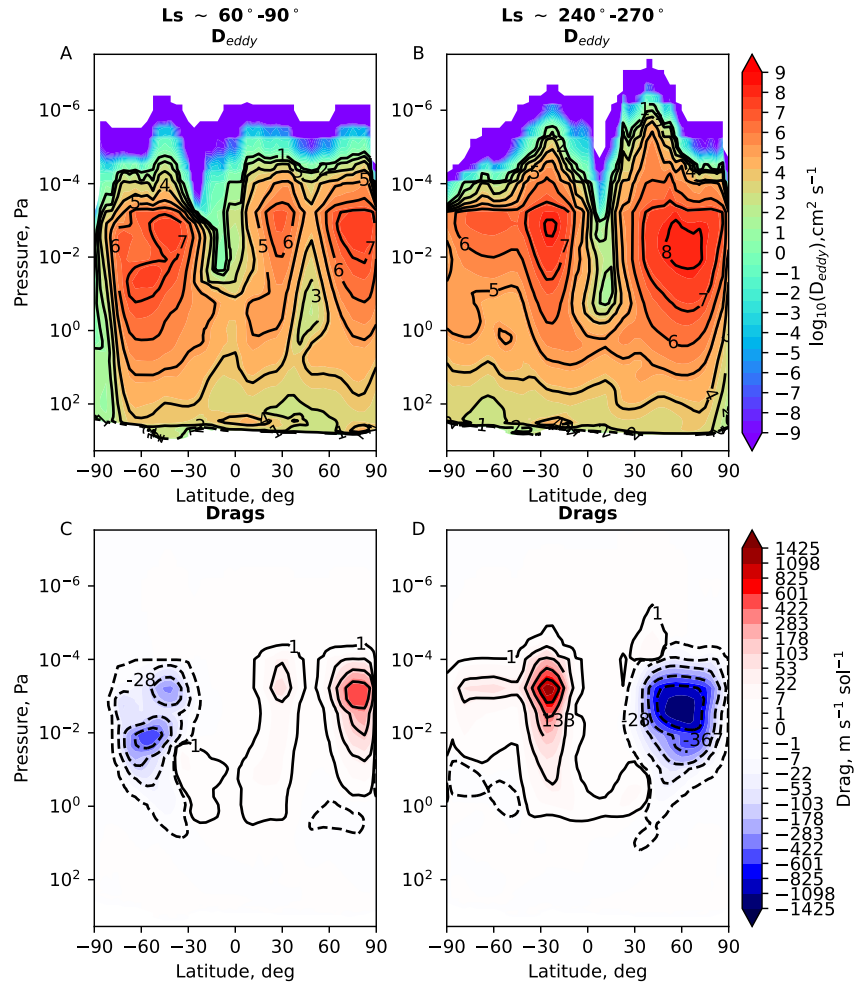

Figure 2. Monthly-averaged zonal averaged D_{eddy} ($cm^2\ s^{-1}$, upper panels) and zonal drags ($m\ s^{-1}\ sol^{-1}$, lower panels) during clear-sky (Ls 60°-90°) and dusty seasons (240°-270°), MY32. Note that the D_{eddy} is plotted in $\log_{10}$ and the contour lines of the drags are nonlinear and not shown for values less than $10^0\ cm^2\ s^{-1}$.

The magnitudes of the eddy diffusivity below 60 km described here are one or two orders less than the values retrieved from observations (Anderson & Leovy, 1978; Rodrigo et al., 1990; Rosenqvist & Chassefière, 1995; Shimazaki, 1989). The orographic GWs induced mixing could explain this discrepancy since this type of wave is thought to be dominant in the lower atmosphere (Forget et al., 1999; Lott & Miller, 1997). In contrast, the eddy diffusivity of the upper atmosphere is consistent with multiple observations (Sprague et al., 2004; Yoshida et al., 2022).

4.2.2. Comparison With MCS

The Mars PCM converges to the MCS temperatures below 100 km (Figure 3a) with turning on the GWs. A middle atmosphere warming structure lies in the simulations between 10^0 and 10^{-1} Pa (Figures 3b–3d). The strip may result from an inaccurate representation of the shortwave CO_2 heating that is represented by a wide-band scheme (González-Galindo et al., 2009). The waves are wrongly saturated due to the structure and interact with the downward branch of the Hadley Cell. Consequently, the structure becomes even warmer in the southern hemisphere with gravity waves (Figures 3c and 3d) compared to the GWoff case (Figure 3b). Apart from that, the model predicts a high-latitude middle atmosphere "cold pocket" (Heavens et al., 2022; Spiga et al., 2012) with gravity waves (Figures 3c and 3d). The comparisons between simulations (Figures 3b, 3c, 3f, and 3g) and observations (Figures 3a and 3e) have been detailed in (J. Liu et al., 2023). We will focus on the mixing effects in the following.

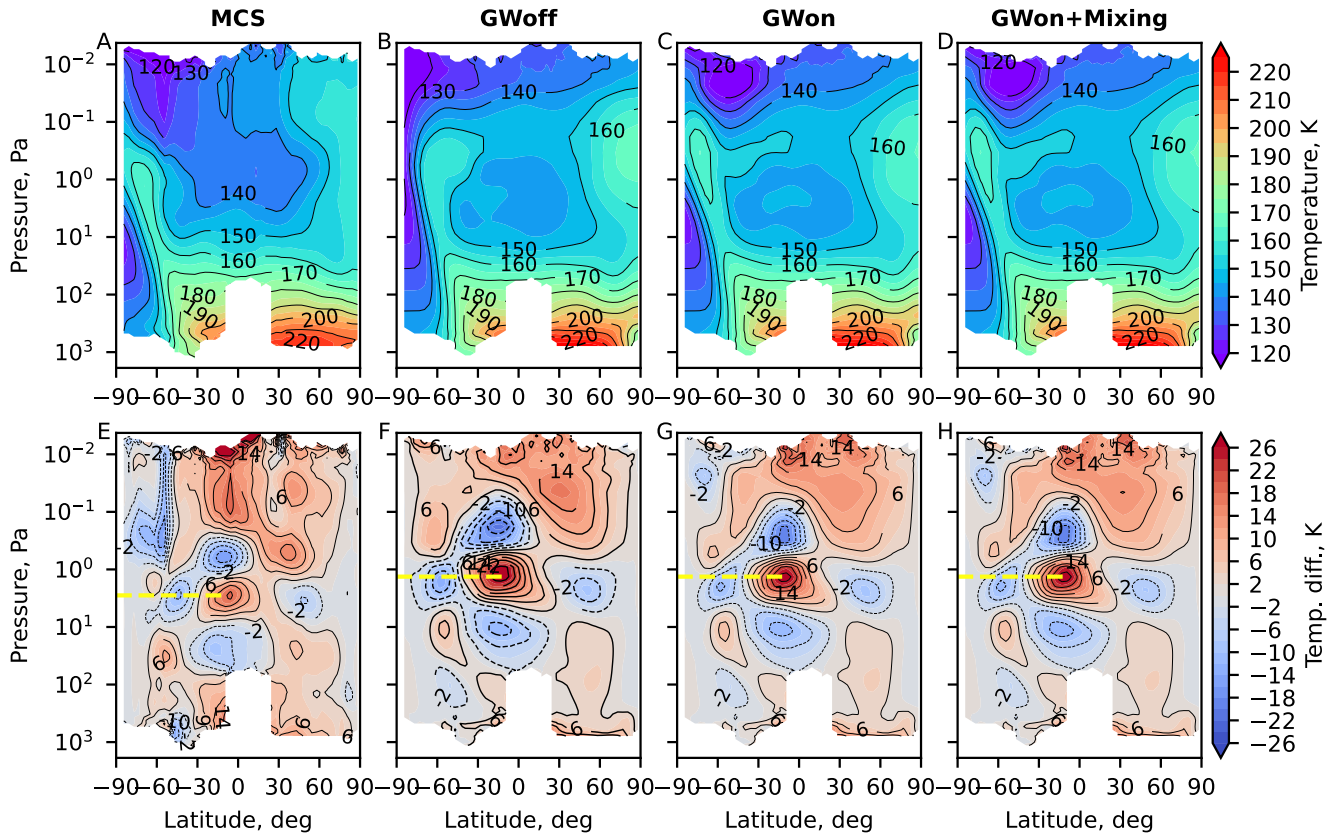

Figure 3. Monthly averaged zonal averaged temperature (K) and diurnal tide (K), Ls 60°-90°, MY32. The temperature in upper panels: (a) MCS observations; (b) simulations with GWs, (c) without GWs, and (d) GWs + mixing. Lower panels (e-h) are corresponding diurnal tides.

The wave-induced mixing has minor effects on the temperature (Figure 3d) and tide (Figure 3h) below 100 km (10^{-2} Pa) compared to the GWon cases (Figures 3c and 3g). The mixing effects on thermal structure are also minor during the dusty seasons (Figure 4). This indicates that the mixing-induced drags (Equation 50) are moderate, which is consistent with the linear damping assumption. In addition, the mixing flux is not accompanied by transferring of net heating flux, which is suggested by the Tylor-Goldstein equations and energy conservation.

4.2.3. Impacts on Tracers

There are 43 tracers evaluated in the model. We chose to show four of them here, including CO, Ar, H_2O vapor, and atomic Oxygen (O). CO and Ar are considered long-existing chemical species whose lifetimes are far longer than the time scale of the eddy mixing (Jakosky et al., 2017; Rodrigo et al., 1990; Sprague et al., 2004). While O has an extremely short lifetime due to its active nature in photochemistry (Mahaffy, Benna, Elrod, et al., 2015). Additionally, H_2O is the key to understanding Mars's habitability evolution. We define a variable χ_q to describe the mixing effects on tracers q, such as,

$$\chi_q = 10^{-6}\left|w'_{mix}n_q^{mix} - w'_{GWon}n_q^{GWon}\right| \tag{54}$$

where w'_{mix} and n_q^{mix} are simulated vertical velocity and tracer number density with the mixing scheme turned on (GWon + mixing), respectively; w'_{GWon} and n_q^{GWon} are variables simulated with only GWs; the 10^{-6} term transfers cm^{-3} into m^{-3} thus χ_q has a unit of m s^{-1} m^{-3}. Therefore, χ_q represents the differences in tracers' vertical fluxes between mixing turning on and off. Figure 5 shows χ_q (in $\log_{10}(\chi_q)$ for convenience) in terms of CO, Ar, H_2O vapor, and atomic Oxygen (O).

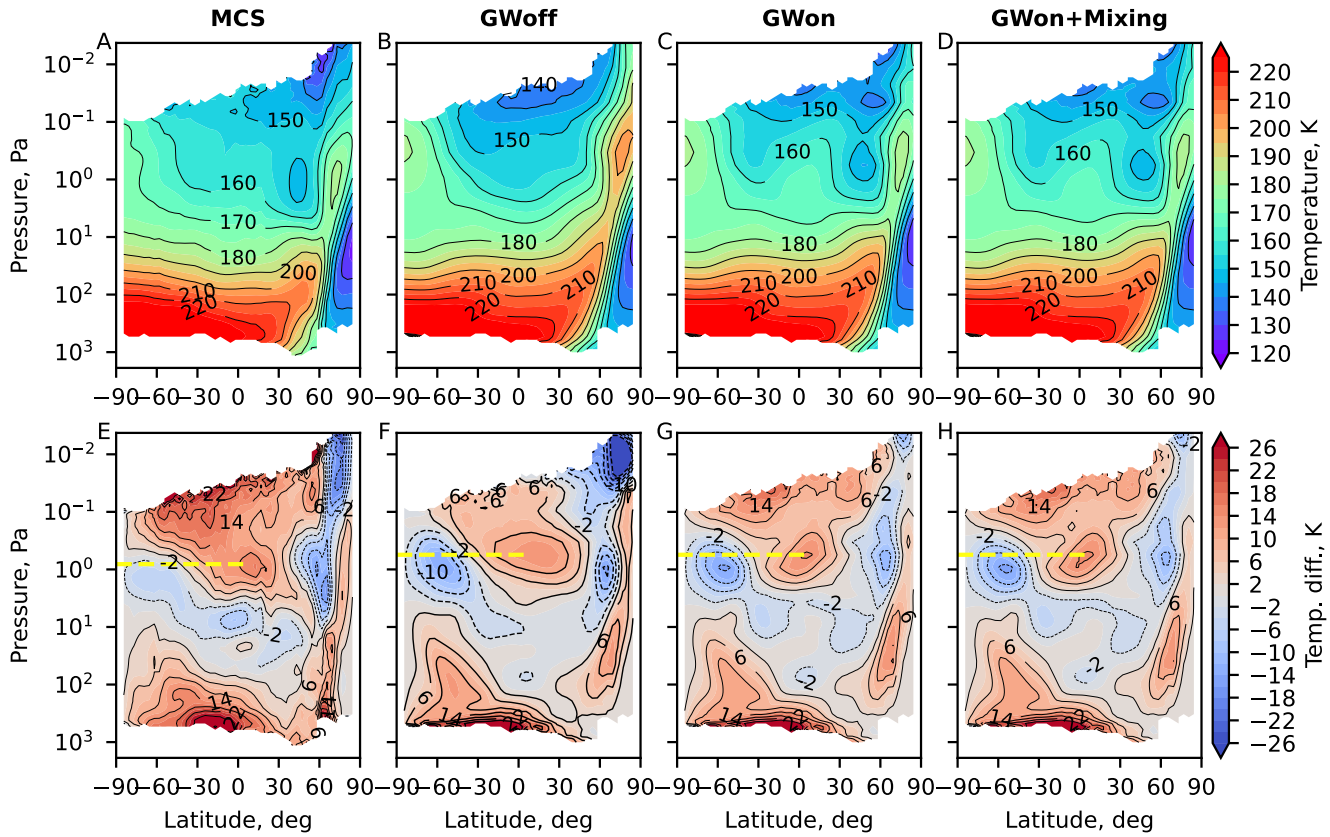

Figure 4. Similar to Figure 3, but for Ls 240°-270°, MY32.

The χ_{CO} (Figure 5a) experiences a fractal distribution of 10^2-10^4 below 60 km during clear-sky seasons, indicating number density variations of 10^7-10^9 cm^{-3} (assuming the averaged w' equals 2.5 m s^{-1}). Similarly, the upper atmospheric n_{CO} variations are of 10^5-10^8 cm^{-3}. This applies to dusty seasons as well (Figure 5e). A similar situation happens for Ar (Figures 5b and 5f).

A lack of middle atmosphere to lower thermosphere H_2O vapor exchange occurs during Ls 60°-90° (Figure 5c) due to a relatively weaker Hadley circulation (J. Liu et al., 2023), in which the density variations lie between 10^4-10^6 cm^{-3}. In contrast, the variations increase to 10^5-10^7 cm^{-3} during dusty seasons (Figure 5g). Additionally, the variations of O are minor below 30 km (Figures 5d and 5h) due to the low O density in these regions. The variations are equivalent to the stable gases above 30 km.

The χ_q collocates with the asymmetric Mars Hadley Cell that is reflected by the temperatures (Figures 3 and 4). It causes intensive mass exchanges in the descending branches of HC, that is, the southern hemispheric polar region during Ls 60°-90°. Likewise, the intense matter (CO_2 condensation) exchanges happen at the northern polar area during Ls 240°-270°. Therefore, it is not very surprising to observe Ar enhancement (a kind of "alien weather" as termed by Forget (2004)) in the observations (Sprague et al., 2004) during the clear-sky southern high-latitude region as shown in Figure 5b.

The mixing on tracers is coupled with the dust activities (lower panels of Figure 5). The altitudes of the mixing increase by 20–40 km during dusty seasons, facilitating the transport of H_2O into the thermosphere much more easily (Figure 5g). The mixing effects are stronger during Ls 240°-270°. Therefore, the H_2O spikes in the lower thermosphere would be common during the dusty seasons, which have been noticed by observations (M. S. Chaffin et al., 2021; Fedorova et al., 2020; Stone et al., 2020). The atmosphere experiences an overall expansion during the dusty seasons, in which the atmospheric densities are increased at a given altitude. This decreases the kinematic viscosity $\nu = \mu/\rho$ (Equation 28), favoring the waves' momentum deposition at higher altitudes. On the other hand, the density increases, and the wind perturbations have strengthened the waves' EP-flux (Equation 3),

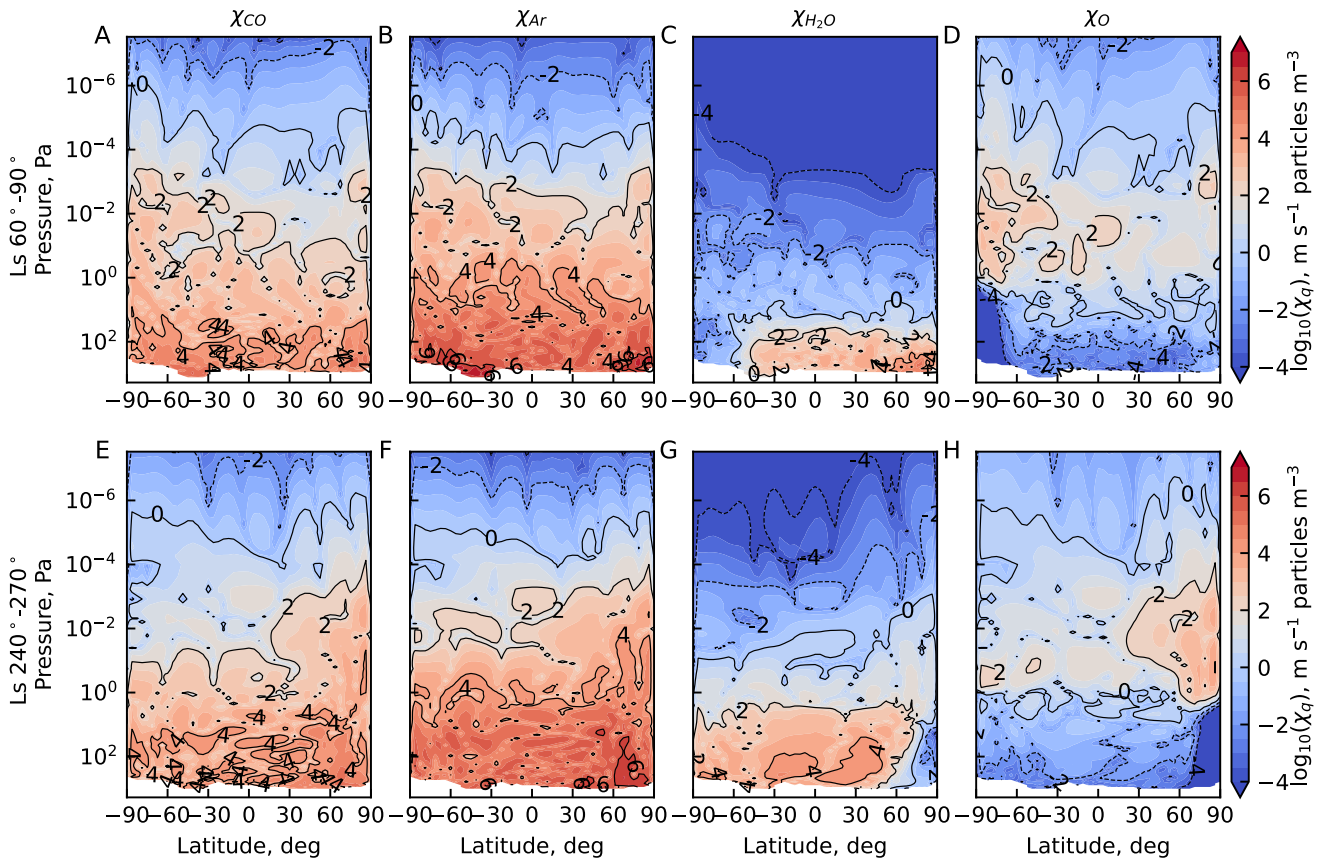

Figure 5. Monthly-averaged zonal averaged χ_q with q = CO, Ar, H_2O(vapor), O, MY32. Upper panels: χ_q during Ls 60°-90°. Lower panels: χ_q during Ls 240°-270°.

leading to higher momentum intensity during the dust seasons (Figure 2d). This generates higher D_{eddy} values (Figure 2b) than the eddy diffusivity during clear-sky seasons (Figure 2a). It causes intensive and almost instantaneous mixing and transport of tracers between the middle atmosphere and the thermosphere during the dusty seasons.

4.2.4. Comparison With NGIMS

Figure 6 shows the density comparisons between NGIMS-measured five neutrals (CO_2, N_2, Ar, CO, O) and the simulations with and without mixing at altitudes of 180 km during MY32 to MY35. The correlated coefficients between the observations and simulations are shown in Figure 6f for the CO2 case (Figure 6a). The observational geometry is illustrated in the bottom panel (Figure 6g). Note that the simulations are instantaneous outputs every 2 hr. However, the observations are high-frequency samples (1 Hz) during short periods (≈300 s, inbound). The outputs of the simulations are interpolated linearly to compare with the observations.

A net increase in all of the five species is caused by the mixing and related chemical processes (Figure 6). The large simulation-observation discrepancies in MY33, MY34, and MY35 during Ls 0°-180° are compensated for by the mixing effects (Figures 6a–6c). The increase or decrease of the upper densities is a complicated response of the upper atmosphere to the dynamics induced by the drags and turbulence of gravity waves.

The abundance of CO_2 is improved due to the turbulence of the waves (Figure 6a), leading to a better matching with the observations during all MYs except MY34. The model has an overestimate of upper atmosphere density during the global dust event (MY34) due to over-ejected dust. The N_2 and Ar (Figures 6b and 6c) follow the similar trends as CO_2. NGIMS has difficulties in separating CO from N_2 (Benna & Lyness, 2014), thus resulting in overlapped values in the observations (Figure 6d). The simulations that include mixing show a higher overall correlation with NGIMS compared to the GWon-NGIMS correlations (Figure 6f).

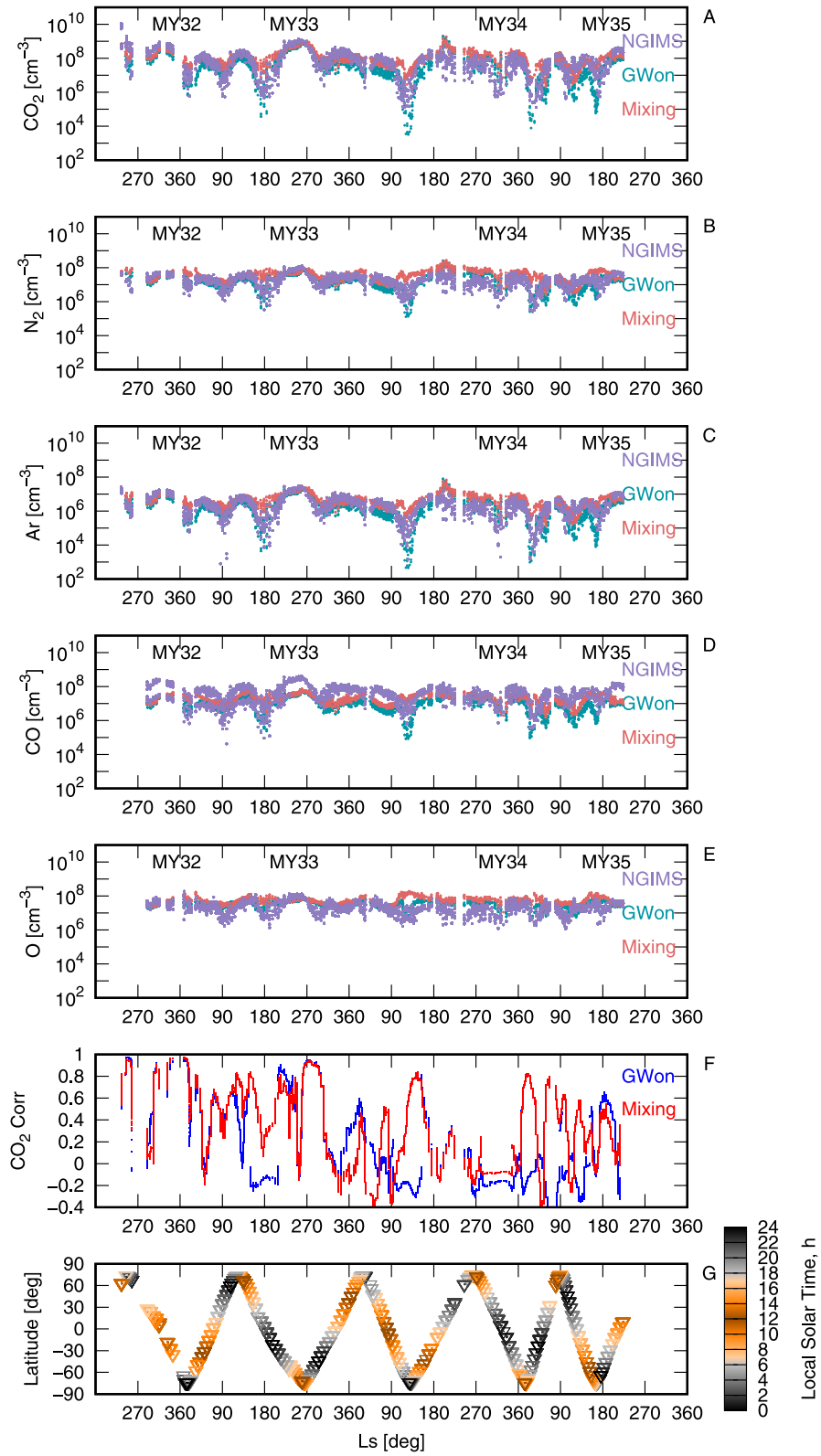

Figure 6. Neutrals abundance (cm^{-3}) at altitudes of 180 ± 0.1 km, from NGIMS (purple), GWon (shallow blue), and Mixing (shallow red), MY32 to MY35. (a) CO_2; (b) N_2; (c) Ar; (d) CO; and (e) O; (f) correlated coefficients of (a) between NGIMS and simulations (GWon in blue and Mixing in red); (g) observational geometry. The duplicated observations in (d) are due to the difficulty in separating CO from N_2 by NGIMS.

Besides, the reverse evolution in the simulations (Ls 300°, MY33 to Ls 120°, MY34; Ls after 200°, MY35) may indicate an overconsumption of CO due to chemical reactions during the day (LST 06–18 hr, Figure 6g). Figure 6e shows that the simulations lack diurnal variations in atomic oxygen. This may be due to the much longer model output time intervals compared to the extremely short lifetime of atomic oxygen. In addition, all five species are overestimated by the mixing scheme during nighttime. This suggests that the nighttime mixing needs to be weaker and the GWs need to be emitted from a lower altitude to increase the "wind filtering" effects (J. Liu et al., 2025).

5. Summary

The turbulence triggered by non-orographic Gravity Waves (GWs) is implemented in the Mars Planetary Climate Model (Mars PCM) using stochastic parametrization. We revisit and refine the formalisms of R. S. Lindzen (1981), Holton (1982), and Weinstock (1982) to better capture the mixing of non-orographic gravity waves. The new formalism integrates with a stochastic GW scheme designed by Lott et al. (2012), which operates across the entire atmosphere in the Mars PCM (J. Liu et al., 2023). The scheme has been tested with the Mars PCM. Simulations are compared with temperatures from the Mars Climate Sounder (MCS, onboard Mars Reconnaissance Orbiter) below 100 km, and abundances from the Neutral Gas and Ion Mass Spectrometer (NGIMS, onboard the Mars Atmosphere and Volatile EvolutioN mission) in the upper atmosphere.

A stochastic turbulence scheme for non-orographic GWs is developed and integrated into the framework of J. Liu et al. (2023), with both the GW and turbulence formulations derived from a refined Non-Superadiabatic Principle (NSP).

The concept of NSP originally links GW-induced turbulence to thin superadiabatic layers caused by wave saturation Hodges (1967, 1969), R. S. Lindzen (1981), Holton (1982). The idea has been refined without major changes to the formulations. Under the new parameterization, turbulence is assumed to arise from wave momentum release. This allows turbulence to be generated throughout all altitudes, rather than only at the saturation level.

The refined NSP can describe wave saturation and saturated turbulence via the energy equation consistently. By applying linear damping to represent turbulent dissipation, it suggests that the R. S. Lindzen (1981) formulation is suitable to represent the saturated turbulence at z_b. The Holton (1982) approach works above z_b. The empirical formula applied below z_b is in accordance with the refined NSP. Thus, the wave-induced eddy diffusivity can be given by a comprehensive formula for all atmospheric layers. The coefficient is proportional to the divergence of the GW's EP flux as suggested by the refined NSP.

The turbulent diffusion is represented by the averaged diffusion flux of a wave ensemble in zonal winds, tracers, and potential temperature. The flux divergences are then added to the mean fields using a first-order Auto-Regressive algorithm. This approach was first proposed by Lott et al. (2012) to capture the drags of a wave ensemble.

Therefore, the non-orographic GW parameterizations of Lott et al. (2012) and J. Liu et al. (2023) are theoretically integrated with the new turbulence scheme via refined NSP and linear damping in the wave energy equation.

Simulations conducted by Mars PCM show that a maximum of 10^6 to 10^7 cm^2 s^{-1} eddy diffusion coefficient has been triggered at 10^0 to 10^{-4} Pa due to the momentum released from the waves during the clear-sky seasons. The value hits 10^7 to 10^8 (or even 10^9) cm^2 s^{-1} during dusty seasons due to the enhanced intensity of the momentum and wave-breaking altitude.

This seasonally and spatially varying eddy diffusion plays a key role in shaping the upper atmosphere, especially near the turbopause—the transition region where eddy and molecular diffusion are of similar magnitude. Mars has a turbopause that varies from 70 to 140 km, dependent on latitude and seasons, implying the key role of GW-induced turbulence in atmosphere escape (Jakosky et al., 2017; Slipski et al., 2018).

The turbulence has minor effects on the model temperature and tide, suggesting no net thermal energy is emitted. Therefore, the scheme conserves energy.

The estimated turbulence has a strong vertical transport effect on the tracers such as CO, Ar, H_2O (vapor), and O. This can explain some instantaneous tracers' density fluctuations observed by observations (Stone et al., 2020).

Comparisons with NGIMS suggest that the turbulence from non-orographic GWs can regulate the upward/downward transport of atmospheric species.

The overestimate of nighttime upper atmospheric abundances may be caused by weak GW buildup during the night. This leads to insufficient cooling. The problem occurs when waves are launched from an averaged planetary boundary layer (PBL). A better approach is to vary the source altitude with the diurnal cycle of the Martian PBL (J. Liu et al., 2025). More advanced mixing implementation considering the tracers' density gradients will be considered in the future.

Data Availability Statement

The NGIMS density data sets (Benna & Lyness, 2014) and MCS temperature profiles (McCleese & Schofield, 2008) analyzed in this study are publicly accessible through the NASA Planetary Data System. Simulations were conducted using the Mars Planetary Climate Model (PCM), freely available at svn.lmd.jussieu.fr/Planeto/trunk, with revision r3263. All results are reproducible using the provided files and instructions in J. Liu and Millour (2025).

Acknowledgments
J. Liu acknowledges the National Natural Science Foundation of China (Grant 42241115). We also extend our gratitude to GENCI-CINES for providing HPC computing resources (Grant A0160110391). We acknowledge funding from the European Research Council (ERC) under the European Union's Horizon 2020 Research and Innovation Program (Grant 835275, project *Mars Through Time*). We acknowledge the constructive efforts of Prof. Lei Jiuhou and another anonymous reviewer, who took the time to review such a complicated technical paper.

References

Anderson, E., & Leovy, C. (1978). Mariner 9 television limb observations of dust and ice hazes on mars. *Journal of the Atmospheric Sciences*, *35*(4), 723–734. https://doi.org/10.1175/1520-0469(1978)035⟨0723:MTLOOD⟩2.0.CO;2

Barnes, J. R., Walsh, T. D., & Murphy, J. R. (1996). Transport timescales in the Martian atmosphere: General circulation model simulations. *Journal of Geophysical Research: Planets*, *101*(E7), 16881–16889. https://doi.org/10.1029/96JE00500

Beasley, W. H., & Hodges, R., Jr. (1973). Wave-induced eddy diffusion coefficients in the upper atmosphere of mars. *Journal of Geophysical Research*, *78*(25), 5425–5428. https://doi.org/10.1029/JA078i025p05425

Benna, M., Bougher, S., Lee, Y., Roeten, K., Yiğit, E., Mahaffy, P., & Jakosky, B. (2019). Global circulation of Mars' upper atmosphere. *Science*, *366*(6471), 1363–1366. https://doi.org/10.1126/science.aax1553

Benna, M., & Lyness, E. (2014). MAVEN neutral gas and ion Mass spectrometer Data [Dataset]. *NASA Planetary Data System*. https://doi.org/10.17189/1518931

Chaffin, M., Deighan, J., Schneider, N., & Stewart, A. (2017). Elevated atmospheric escape of atomic hydrogen from mars induced by high-altitude water. *Nature Geoscience*, *10*(3), 174–178. https://doi.org/10.1038/ngeo2887

Chaffin, M. S., Kass, D., Aoki, S., Fedorova, A., Deighan, J., Connour, K., et al. (2021). Martian water loss to space enhanced by regional dust storms. *Nature Astronomy*, *5*(10), 1036–1042. https://doi.org/10.1038/s41550-021-01425-w

Creasey, J. E., Forbes, J. M., & Keating, G. M. (2006). Density variability at scales typical of gravity waves observed in Mars' thermosphere by the MGS accelerometer. *Geophysical Research Letters*, *33*(22), L22814. https://doi.org/10.1029/2006GL027583

De la Cámara, A., Lott, F., & Hertzog, A. (2014). Intermittency in a stochastic parameterization of nonorographic gravity waves. *Journal of Geophysical Research: Atmospheres*, *119*(21), 11–905. https://doi.org/10.1002/2014JD022002

England, S. L., Liu, G., Yiğit, E., Mahaffy, P. R., Elrod, M., Benna, M., et al. (2017). MAVEN NGIMS observations of atmospheric gravity waves in the Martian thermosphere. *Journal of Geophysical Research: Space Physics*, *122*(2), 2310–2335. https://doi.org/10.1002/2016JA023475

Fedorova, A. A., Montmessin, F., Korablev, O., Luginin, M., Trokhimovskiy, A., Belyaev, D. A., et al. (2020). Stormy water on mars: The distribution and saturation of atmospheric water during the dusty season. *Science*, *367*(6475), 297–300. https://doi.org/10.1126/science.aay9522

Forget, F. (2004). Alien weather at the poles of mars. *Science*, *306*(5700), 1298–1299. https://doi.org/10.1126/science.1105669

Forget, F., Hourdin, F., Fournier, R., Hourdin, C., Talagrand, O., Collins, M., et al. (1999). Improved general circulation models of the Martian atmosphere from the surface to above 80 km. *Journal of Geophysical Research: Planets*, *104*(E10), 24155–24175. https://doi.org/10.1029/1999JE001025

Fritts, D. C. (1984). Gravity wave saturation in the middle atmosphere: A review of theory and observations. *Reviews of Geophysics*, *22*(3), 275–308. https://doi.org/10.1029/RG022i003p00275

Fritts, D. C., & Alexander, M. J. (2003). Gravity wave dynamics and effects in the middle atmosphere. *Reviews of Geophysics*, *41*(1). https://doi.org/10.1029/2001RG000106

Fritts, D. C., Wang, L., & Tolson, R. H. (2006). Mean and gravity wave structures and variability in the Mars upper atmosphere inferred from Mars Global Surveyor and Mars Odyssey aerobraking densities. *Journal of Geophysical Research: Space Physics*, *111*(A12), A12304. https://doi.org/10.1029/2006JA011897

Garcia, R. R., & Solomon, S. (1985). The effect of breaking gravity waves on the dynamics and chemical composition of the mesosphere and lower thermosphere. *Journal of Geophysical Research: Atmospheres*, *90*(D2), 3850–3868. https://doi.org/10.1029/JD090iD02p03850

González-Galindo, F., Forget, F., López-Valverde, M., & Angelats i Coll, M. (2009). A ground-to-exosphere Martian general circulation model: 2. Atmosphere during solstice conditions—Thermospheric polar warming. *Journal of Geophysical Research: Planets*, *114*(E8), E08004. https://doi.org/10.1029/2008JE003277

Heavens, N. G., Pankine, A., Battalio, J. M., Wright, C., Kass, D. M., Kleinböhl, A., et al. (2022). Mars climate sounder observations of gravity-wave activity throughout Mars's lower atmosphere. *The Planetary Science Journal*, *3*(3), 57. https://doi.org/10.3847/PSJ/ac51ce

Hines, C. (1974). Eddy diffusion coefficients due to instabilities in internal gravity waves. *Geophysical Monograph Series*, *18*(19), 423–428. https://doi.org/10.1029/JA075i019p03937

Hodges, R., Jr. (1967). Generation of turbulence in the upper atmosphere by internal gravity waves. *Journal of Geophysical Research*, *72*(13), 3455–3458. https://doi.org/10.1029/JZ072i013p03455

Hodges, R., Jr. (1969). Eddy diffusion coefficients due to instabilities in internal gravity waves. *Journal of Geophysical Research*, *74*(16), 4087–4090. https://doi.org/10.1029/ja074i016p04087

Holton, J. R. (1982). The role of gravity wave induced drag and diffusion in the momentum budget of the mesosphere. *Journal of the Atmospheric Sciences*, *39*(4), 791–799. https://doi.org/10.1175/1520-0469(1982)039⟨0791:TROGWI⟩2.0.CO;2

Holton, J. R. (1983). The influence of gravity wave breaking on the general circulation of the middle atmosphere. *Journal of the Atmospheric Sciences*, *40*(10), 2497–2507. https://doi.org/10.1175/1520-0469(1983)040⟨2497:TIOGWB⟩2.0.CO;2

Holton, J. R., & Schoeberl, M. R. (1988). The role of gravity wave generated advection and diffusion in transport of tracers in the mesosphere. *Journal of Geophysical Research: Atmospheres*, *93*(D9), 11075–11082. https://doi.org/10.1029/JD093iD09p11075

Imamura, T., Watanabe, A., & Maejima, Y. (2016). Convective generation and vertical propagation of fast gravity waves on mars: One-and two-dimensional modeling. *Icarus*, *267*, 51–63. https://doi.org/10.1016/j.icarus.2015.12.005

Jakosky, B. M., Slipski, M., Benna, M., Mahaffy, P., Elrod, M., Yelle, R., et al. (2017). Mars' atmospheric history derived from upper-atmosphere measurements of 38ar/36ar. *Science*, *355*(6332), 1408–1410. https://doi.org/10.1126/science.aai7721

Leovy, C. B. (1982). Control of the homopause level. *Icarus*, *50*(2–3), 311–321. https://doi.org/10.1016/0019-1035(82)90128-2

Li, Y., Liu, J., & Jin, S. (2021). Horizontal internal gravity waves in the Mars upper atmosphere from MAVEN ACC and NGIMS measurements. *Journal of Geophysical Research: Space Physics*, *126*(1), e2020JA028378. https://doi.org/10.1029/2020JA028378

Lindzen, R., & Forbes, J. (1983). Turbulence originating from convectively stable internal waves. *Journal of Geophysical Research: Oceans*, *88*(C11), 6549–6553. https://doi.org/10.1029/JC088iC11p06549

Lindzen, R. S. (1981). Turbulence and stress owing to gravity wave and tidal breakdown. *Journal of Geophysical Research: Oceans*, *86*(C10), 9707–9714. https://doi.org/10.1029/JC086iC10p09707

Liu, H.-L. (2021). Effective vertical diffusion by atmospheric gravity waves. *Geophysical Research Letters*, *48*(1), e2020GL091474. https://doi.org/10.1029/2020GL091474

Liu, J., Jin, S., & Li, Y. (2019). Seasonal variations and global wave distributions in the Mars thermosphere from MAVEN and multisatellites accelerometer-derived Mass densities. *Journal of Geophysical Research: Space Physics*, *124*(11), 9315–9334. https://doi.org/10.1029/2019JA026720

Liu, J., & Millour, E. (2025). Data for 'A stochastic parameterization of non-orographic1 gravity waves induced mixing for Mars Planetary Climate Model [Dataset]. *Mendeley Data*. https://doi.org/10.17632/7krjshk8tj.1

Liu, J., Millour, E., Forget, F., Gilli, G., Lott, F., Bardet, D., et al. (2023). A surface to exosphere non-orographic gravity wave parameterization for the Mars Planetary Climate Model. *Journal of Geophysical Research: Planets*, *128*(7), e2023JE007769. https://doi.org/10.1029/2023JE007769

Liu, J., Millour, E., Forget, F., Gilli, G., Lott, F., Bardet, D., & Galindo, G. (2025). Diurnal cycle of non-orographic gravity waves' source altitudes and its impacts: Tests with Mars Planetary Climate Model. *Journal of Geophysical Research: Planets*, *130*(7), e2024JE008880. https://doi.org/10.1029/2024JE008880

Lott, F., & Guez, L. (2013). A stochastic parameterization of the gravity waves due to convection and its impact on the equatorial stratosphere. *Journal of Geophysical Research: Atmospheres*, *118*(16), 8897–8909. https://doi.org/10.1002/jgrd.50705

Lott, F., Guez, L., & Maury, P. (2012). A stochastic parameterization of non-orographic gravity waves: Formalism and impact on the equatorial stratosphere. *Geophysical Research Letters*, *39*(6), L06807. https://doi.org/10.1029/2012GL051001

Lott, F., & Miller, M. J. (1997). A new subgrid-scale orographic drag parametrization: Its formulation and testing. *Quarterly Journal of the Royal Meteorological Society*, *123*(537), 101–127. https://doi.org/10.1002/qj.49712353704

Mahaffy, P. R., Benna, M., Elrod, M., Yelle, R. V., Bougher, S. W., Stone, S. W., & Jakosky, B. M. (2015). Structure and composition of the neutral upper atmosphere of Mars from the MAVEN NGIMS investigation. *Geophysical Research Letters*, *42*(21), 8951–8957. https://doi.org/10.1002/2015GL065329

Mahaffy, P. R., Benna, M., King, T., Harpold, D. N., Arvey, R., Barciniak, M., et al. (2015). The neutral gas and ion mass spectrometer on the Mars atmosphere and volatile evolution mission. *Space Science Reviews*, *195*(1), 49–73. https://doi.org/10.1007/s11214-014-0091-1

McCleeseSchofield. (2008). MRO Mars climate sounder derived Data records V1.0. NASA planetary Data system [Dataset]. *NASA Planetary Data System*. https://doi.org/10.17189/P73K-XY37

McElroy, M., Kong, T., Yung, Y., & Nier, A. (1976). Composition and structure of the Martian upper atmosphere: Analysis of results from Viking. *Science*, *194*(4271), 1295–1298. https://doi.org/10.1126/science.194.4271.1295

McElroy, M. B., & Donahue, T. M. (1972). Stability of the martian atmosphere. *Science*, *177*(4053), 986–988. https://doi.org/10.1126/science.177.4053.986

Nakagawa, H., Terada, N., Jain, S. K., Schneider, N. M., Montmessin, F., Yelle, R. V., et al. (2020). Vertical propagation of wave perturbations in the middle atmosphere on Mars by MAVEN/IUVS. *Journal of Geophysical Research: Planets*, *125*(9), e2020JE006481. https://doi.org/10.1029/2020JE006481

Nappo, C. J. (2013). An introduction to atmospheric gravity waves: The linear theory (Vol. *102*). https://doi.org/10.1016/B978-0-12-385223-6.00002-1

Nier, A., & McElroy, M. (1976). Structure of the neutral upper atmosphere of mars: Results from viking 1 and viking 2. *Science*, *194*(4271), 1298–1300. https://doi.org/10.1126/science.194.4271.1298

Rodrigo, R., Álvarez, E. G., González, M. L., & Valverde, M. L. (1990). Estimates of eddy diffusion coefficient in the Mars' atmosphere. *Atmósfera*, *3*(1), 31–43.

Roeten, K., Bougher, S., Yigit, E., Medvedev, A., Benna, M., & Elrod, M. (2022). Impacts of gravity waves in the Martian thermosphere: The Mars Global Ionosphere-Thermosphere Model coupled with a whole atmosphere gravity wave scheme. *Journal of Geophysical Research: Planets*, *127*(12), e2022JE007477. https://doi.org/10.1029/2022JE007477

Rosenqvist, J., & Chassefière, E. (1995). A reexamination of the relationship between eddy mixing and O_2 in the Martian middle atmosphere. *Journal of Geophysical Research: Planets*, *100*(E3), 5541–5551. https://doi.org/10.1029/95JE00324

Shimazaki, T. (1989). Photochemical stability of co2 in the Martian atmosphere reevaluation of the eddy diffusion coefficient and the role of water vapor. *Journal of Geomagnetism and Geoelectricity*, *41*(3), 273–301. https://doi.org/10.5636/jgg.41.273

Slipski, M., Jakosky, B., Benna, M., Elrod, M., Mahaffy, P., Kass, D., et al. (2018). Variability of Martian turbopause altitudes. *Journal of Geophysical Research: Planets*, *123*(11), 2939–2957. https://doi.org/10.1029/2018JE005704

Spiga, A., González-Galindo, F., López-Valverde, M.-Á., & Forget, F. (2012). Gravity waves, cold pockets and CO_2 clouds in the Martian mesosphere. *Geophysical Research Letters*, *39*(2). https://doi.org/10.1029/2011GL050343

Sprague, A., Boynton, W., Kerry, K., Janes, D., Hunten, D., Kim, K., et al. (2004). Mars' south polar AR enhancement: A tracer for south polar seasonal meridional mixing. *Science*, *306*(5700), 1364–1367. https://doi.org/10.1126/science.1098496

Stone, S. W., Yelle, R. V., Benna, M., Elrod, M. K., & Mahaffy, P. R. (2018). Thermal structure of the Martian upper atmosphere from MAVEN NGIMS. *Journal of Geophysical Research: Planets*, *123*(11), 2842–2867. https://doi.org/10.1029/2018JE005559

Stone, S. W., Yelle, R. V., Benna, M., Lo, D. Y., Elrod, M. K., & Mahaffy, P. R. (2020). Hydrogen escape from Mars is driven by seasonal and dust storm transport of water. *Science*, *370*(6518), 824–831. https://doi.org/10.1126/science.aba5229

Strobel, D. F. (1989). Constraints on gravity wave induced diffusion in the middle atmosphere. *Pure and Applied Geophysics*, *130*(2–3), 533–546. https://doi.org/10.1007/BF00874473

Strobel, D. F., Apruzese, J. P., & Schoeberl, M. R. (1985). Energy balance constraints on gravity wave induced eddy diffusion in the mesosphere and lower thermosphere. *Journal of Geophysical Research: Atmospheres*, *90*(D7), 13067–13072. https://doi.org/10.1029/JD090iD07p13067

Théodore, B., Lellouch, E., Chassefière, E., & Hauchecorne, A. (1993). Solstitial temperature inversions in the Martian middle atmosphere: Observational clues and 2-D modeling. *Icarus*, *105*(2), 512–528. https://doi.org/10.1006/icar.1993.1145

Vals, M., Spiga, A., Forget, F., Millour, E., Montabone, L., & Lott, F. (2019). Study of gravity waves distribution and propagation in the thermosphere of Mars based on MGS, ODY, MRO and MAVEN density measurements. *Planetary and Space Science*, *178*, 104708. https://doi.org/10.1016/j.pss.2019.104708

Von Zahn, U., Fricke, K., Hunten, D., Krankowsky, D., Mauersberger, K., & Nier, A. (1980). The upper atmosphere of Venus during morning conditions. *Journal of Geophysical Research: Space Physics*, *85*(A13), 7829–7840. https://doi.org/10.1029/JA085iA13p07829

Weinstock, J. (1982). Nonlinear theory of gravity waves: Momentum deposition, generalized Rayleigh friction, and diffusion. *Journal of the Atmospheric Sciences*, *39*(8), 1698–1710. https://doi.org/10.1175/1520-0469(1982)039⟨1698:NTOGWM⟩2.0.CO;2

Yiğit, E. (2021). Martian water escape and internal waves. *Science*, *374*(6573), 1323–1324. https://doi.org/10.1126/science.abg5893

Yiğit, E., Aylward, A. D., & Medvedev, A. S. (2008). Parameterization of the effects of vertically propagating gravity waves for thermosphere general circulation models: Sensitivity study. *Journal of Geophysical Research: Atmospheres*, *113*(D19), D19106. https://doi.org/10.1029/2008JD010135

Yiğit, E., England, S. L., Liu, G., Medvedev, A. S., Mahaffy, P. R., Kuroda, T., & Jakosky, B. M. (2015). High-altitude gravity waves in the Martian thermosphere observed by MAVEN/NGIMS and modeled by a gravity wave scheme. *Geophysical Research Letters*, *42*(21), 8993–9000. https://doi.org/10.1002/2015GL065307

Yiğit, E., Medvedev, A. S., Benna, M., & Jakosky, B. M. (2021). Dust storm-enhanced gravity wave activity in the Martian thermosphere observed by MAVEN and implication for atmospheric escape. *Geophysical Research Letters*, *48*(5), e2020GL092095. https://doi.org/10.1029/2020GL092095

Yoshida, N., Nakagawa, H., Aoki, S., Erwin, J., Vandaele, A. C., Daerden, F., et al. (2022). Variations in vertical CO/CO_2 profiles in the Martian mesosphere and lower thermosphere measured by the exomars TGO/NOMAD: Implications of variations in eddy diffusion coefficient. *Geophysical Research Letters*, *49*(10), e2022GL098485. https://doi.org/10.1029/2022GL098485